

PNNL-32428

LightMAT - Continuous fiber malleable thermoset composites with sub-1-minute dwell times; validation of impact performance and evaluation of the efficacy of the compression forming process (CRADA 409)

December 2021

Leo Fifield
Michael Larche
Bo Song
Robert Norris
Philip Taynton

DISCLAIMER

This report was prepared as an account of work sponsored by an agency of the United States Government. Neither the United States Government nor any agency thereof, nor Battelle Memorial Institute, nor any of their employees, makes **any warranty, express or implied, or assumes any legal liability or responsibility for the accuracy, completeness, or usefulness of any information, apparatus, product, or process disclosed, or represents that its use would not infringe privately owned rights.** Reference herein to any specific commercial product, process, or service by trade name, trademark, manufacturer, or otherwise does not necessarily constitute or imply its endorsement, recommendation, or favoring by the United States Government or any agency thereof, or Battelle Memorial Institute. The views and opinions of authors expressed herein do not necessarily state or reflect those of the United States Government or any agency thereof.

PACIFIC NORTHWEST NATIONAL LABORATORY
operated by
BATTELLE
for the
UNITED STATES DEPARTMENT OF ENERGY
under Contract DE-AC05-76RL01830

Printed in the United States of America

Available to DOE and DOE contractors from the
Office of Scientific and Technical Information,
P.O. Box 62, Oak Ridge, TN 37831-0062;
ph: (865) 576-8401
fax: (865) 576-5728
email: reports@adonis.osti.gov

Available to the public from the National Technical Information Service
5301 Shawnee Rd., Alexandria, VA 22312
ph: (800) 553-NTIS (6847)
email: orders@ntis.gov <<https://www.ntis.gov/about>>
Online ordering: <http://www.ntis.gov>

LightMAT - Continuous fiber malleable thermoset composites with sub-1-minute dwell times; validation of impact performance and evaluation of the efficacy of the compression forming process (CRADA 409)

December 2021

Leo Fifield
Michael Larche
Bo Song
Robert Norris
Philip Taynton

Prepared for
the U.S. Department of Energy
under Contract DE-AC05-76RL01830

Pacific Northwest National Laboratory
Richland, Washington 99354

Cooperative Research and Development Agreement (CRADA) Final Report

Report Date: 9/28/2021

In accordance with Requirements set forth in the terms of the CRADA, this document is the CRADA Final Report, including a list of Subject Inventions, to be provided to PNNL Information Release who will forward to the DOE Office of Scientific and Technical Information as part of the commitment to the public to demonstrate results of federally funded research.

Cooperative Research and Development Agreement Final Report Report Date: 9/28/2021

Parties to the Agreement:

- Battelle as Operator of Pacific Northwest National Laboratory under its U.S. Department of Energy Contract No. DE-AC05-76RL01830 (PNNL)
- National Technology & Engineering Solutions of Sandia, LLC as Operator of Sandia National Laboratories under its U.S. Department of Energy Contract No. DE-NA-0003525 (Sandia)
- UT- Battelle, LLC as Operator of Oak Ridge National Laboratory under its U.S. Department of Energy Contract No. DE-AC05-00OR22725 (ORNL)
- Mallinda, LLC (Mallinda)

CRADA number:

- PNNL/409 (72473)

CRADA Title:

- Continuous fiber malleable thermoset composites with sub-1-minute dwell times; validation of impact performance and evaluation of the efficacy of the compression forming process.

Responsible Technical Contacts at DOE Labs:

- Leo Fifield (leo.fifield@pnnl.gov)
- Michael Larche (michael.larche@pnnl.gov)
- Bo Song (bsong@sandia.gov)
- Bob Norris (norrisrejr@ornl.gov)

Name and Email Address of POC at Company:

- Philip Taynton (philip@mallinda.com)

DOE Program Office:

- DOE-EERE/VTO

Joint Work Statement Funding Table showing DOE funding commitment:

Funding	Project Year 1	Project Year 2	TOTALS
Government			
DOE's Contribution via Battelle	0	\$225K	\$225K
DOE's Contribution via NTESS	\$87.5K	\$87.5K	\$175K
DOE's Contribution via UT-Battelle	0	\$100K	\$100K
Total Govt.	\$87.5K	\$412.5K	\$500K
Participant			
In-Kind	\$350K	\$150K	\$500K
Funds-In			
FAC			
Total Participant	\$350K	\$150K	\$500K
TOTAL CRADA Value	\$437.5K	\$562.5K	\$1,000K

Acknowledgements and Disclaimer:

This report was prepared as an account of work sponsored by an agency of the United States Government. Neither the United States Government nor any agency thereof, nor Battelle Memorial Institute, nor any of their employees, makes any warranty, express or implied, or assumes any legal liability or responsibility for the accuracy, completeness, or usefulness of any information, apparatus, product, or process disclosed, or represents that its use would not infringe privately owned rights. Reference herein to any specific commercial product, process, or service by trade name, trademark, manufacturer, or otherwise does not necessarily constitute or imply its endorsement, recommendation, or favoring by the United States Government or any agency thereof, or Battelle Memorial Institute. The views and opinions of authors expressed herein do not necessarily state or reflect those of the United States Government or any agency thereof. The Pacific Northwest National Laboratory is operated by Battelle for the U.S. Department of Energy under Contract DE-AC05-76RL01830.

Sandia National Laboratories is a multi-mission laboratory managed and operated by National Technology and Engineering Solutions of Sandia, LLC, a wholly owned subsidiary of Honeywell International, Inc., for the U.S. Department of Energy's National Nuclear Security Administration under contract DE-NA0003525. The views expressed in the article do not necessarily represent the views of the U.S. Department of Energy or the United States Government.

This manuscript has been co-authored by UT-Battelle, LLC, under contract DE-AC05-00OR22725 with the US Department of Energy (DOE). The US government retains and the publisher, by accepting the article for publication, acknowledges that the US government retains a nonexclusive, paid-up, irrevocable, worldwide license to publish or reproduce the published form of this manuscript, or allow others to do so, for US government purposes. DOE will provide public access to these results of federally sponsored research in accordance with the DOE Public Access Plan (<http://energy.gov/downloads/doe-public-access-plan>)

Executive Summary of CRADA Work:

In spite of carbon fiber composite materials' significant impact on light-weighting, performance, and efficiency in the aerospace industry, adoption of these materials has been slow in high-volume industries such as automotive. Two major barriers to adoption are cost and cycle-time. Current approaches to thermoset composite part production are dependent on in-mold curing of thermosets which are not optimal for high volume, high throughput production due to limitations and inefficiencies associated with the in-mold cure itself. In addition, ancillary activities, such as transport and storage of shelf-life-limited uncured, or B-staged prepreg materials typically necessitate refrigerated transport and storage which significantly impacts the economic and energy costs associated with manufacturing. Furthermore, limited out-life means that trimmings cannot typically be used as they partially cure during initial production leading to high scrap rates (+20% is common). Finally, the need to cure in-mold drives cycle times to multiple minutes in the best cases, and 10's of minutes to hours in most cases.

Mallinda is developing polyimine malleable thermoset prepreg composite materials which have excellent mechanical properties (100 GPa tensile modulus, 2 GPA tensile strength, 2.4% elongation at break) and high operating temperatures ($T_g > 200^\circ\text{C}$). At scale, polyimine resins are commensurate in price with commodity epoxy resins. What distinguishes malleable thermoset prepreg from traditional thermoset prepreg materials, is that they are fully cured during Mallinda's roll-to-roll production of prepreg laminate. This results in 5 key value-differentiating benefits. First, it simplifies manufacturing logistics by enabling ambient transportation and storage, and by significantly extending out-life and shelf-life almost indefinitely. Second, elimination of autoclave curing reduces the economic and energy costs to the customer. Third, scrap rates can be reduced as malleable thermoset prepreg materials are directly reusable. Fourth, the manufacturing consolidation step can be roughly 10x faster than traditional thermosets, because the resin is already cured. Parts can be made via compression forming by the application of heat and pressure to quickly vitrify and consolidate a multilayer part – easily leading to sub 3-minute cycle times (at lab scale we have demonstrated a 20 second dwell time, with room for further optimization). Finally, the closed-loop cradle-to-cradle solution-based recyclability of malleable thermoset composites can also contribute significantly to the future of sustainable lightweight materials.

The focus of this project was the development, optimization and validation of malleable thermoset composite materials which exhibit manufacturing cycle times of 3-minute or less, high speed impact performance on par with incumbent technologies, and defect-free consolidation of 3 dimensional parts.

Government funding is required on this project because Mallinda is a start-up company whose focus is the development and scale-up of the described technology for introduction to the transportation segment. Unlike incumbent industry players, Mallinda is bringing a completely new and highly relevant malleable thermoset technology to bear on the problem of high throughput composites. As a small business, Mallinda relies on a combination of government R&D funding and private capital to perform development work.

The national laboratory resources utilized for this project are highly specific to the DOE, and are very difficult to replicate in the private sector:

1. Compression forming and composite manufacturing capabilities

The composite manufacturing and processing capabilities at ORNL is well-connected to the automotive industry through IACMI. The high-pressure molding capability (which is needed for this project) was paired with decades of hands-on knowledge in composite fabrication and innovation. This unique combination of capabilities & expertise is difficult to find in a collaborative environment.

2. High speed impact material characterization

High speed impact material characterization of the composite materials was conducted at Sandia National Laboratories. The Experimental Impact Mechanics Lab (EIML) at Sandia has unique experimental capabilities for material and structure characterization in combined mechanical (from low, intermediate, to high-speed impact) and thermal (-100 to 1200°C) environments. The EIML has over 20-years of experience on dynamic characterization of materials and structures, wave propagation, impact energy absorption and crashworthiness, etc. In this project, the EIML used split Hopkinson (also called Kolsky) compression and tension bars to dynamically characterize the composite materials at different strain rates and environmental temperatures. The proposed test strain rates covered from ~50 to 1000 s⁻¹ (in compression) or 400 s⁻¹ (in tension), which exactly fall into the region of automotive low-to-high-speed collision. The test temperatures ranging from -40 to 60°C were combined with the impact mechanical testing to simulate the automotive environmental temperatures. From this series of tests, the new composite materials were fully evaluated in term of stress-strain response, ultimate strength, elongation at break, and failure/fracture mode at different impact loading speeds and modes, as well as different environmental temperatures. The effects of strain rate and temperature on the material performance was also be determined for developing strain-rate and temperature dependent material models for numerical simulation of automotive collision. In addition, the EIML is also capable of characterizing dynamic fracture toughness to determine the delamination strength of the composite materials under impact loading. All these impact testing data were compared to the mechanical properties of the conventional composites currently used in automotive industries.

3. Non-destructive defect analysis via Scanning Acoustic Microscopy

The combination of measurement and analytics capabilities is unique to the national laboratories in the LightMAT consortium. The collection of measurement capabilities, analytics, experience, and experts separate the national laboratories from industrial counterparts. More specifically, commercial off the shelf scanning acoustic microscopy measurement capabilities do not compare with the custom capabilities developed at PNNL. Although the scanning acoustic microscope at PNNL is a commercially available system, it features modifications that allow it to perform more research-oriented, nonstandard measurements requiring real time data collection, dual probe inspection, improved signal to noise ratio, increased sensitivity, and multi-frequency analysis. Additionally, the teaming of experts in nondestructive examination, simulation & modeling, materials science, and mathematics on prior research efforts produced proven algorithms and analysis approaches that are ready to be applied to new problem spaces. The capabilities, collection of experts and experience of the national laboratories in this project distinctly separate them from industrial counterparts. Having these resources co-located in one organization aided in meeting project objectives.

Overall, access to the resources made available through this project significantly accelerated the project by more than 2x. The time and capital requirements of this project would make it impossible for Mallinda to pursue in the near future without the support of this project. Instead, access to the resources in this project enabled the completion of this complementary project concurrently with Mallinda's 2-year development of high speed R2R composite production capability.

This CRADA resulted in no new inventions to report.

This CRADA resulted in the new network/collaboration of Mallinda's Philip Taynton serving as Industry Mentor for PNNL's RECOVER (High-Performance Bioplastics with High Recyclability and Repairability) Energy i-Corps Team 131.

Technologies/techniques/methodologies furthered through this CRADA include:

- Dynamic tensile and flexural testing capabilities at ORNL
- Dynamic mechanical property characterization of composite materials at various strain rates in compression, tension, and three-point-bending at Sandia
- Ultrasonic analysis of composite defects in 3D parts at PNNL

Summary of Research Results:

Summary of ORNL Research Results

by R. E. Norris, D. L. Erdman, F. Xiong

It is widely acknowledged that composite materials structural failures can be greatly affected by (among others):

- Multiple constituents utilized (fibers, resins, fillers, etc.)
- Levels of each of the constituents utilized
- Arrangements/architecture of the constituents and interfaces
- Design, shape, joints, etc., involved in making the final components
- Quality of each manufacturing step
- Damage present at each stage of life

Being "malleable", one projected advantage of the Mallinda vitrimer material is that it would likely be useful in automotive energy absorption applications. Although doing extensive "qualification" testing of a material still very much in the developmental stage is beyond the scope of this project, Mallinda proposed doing some preliminary dynamic testing of example materials to demonstrate some early results as well as potential techniques for more in-depth comparison of the materials as larger quantities of specimens become available and specific application targets and requirements become better defined.

ORNL has worked with the Automotive Composites Consortium to implement some unique tools for this purpose. Primary tools identified for this work include a High Speed Tensile Tester as shown in Figure 1 and a larger machine known as the Test Machine for Automotive Crashworthiness (TMAC) as shown in Figure 2. Key attributes of this equipment are focused on capability to do constant velocity testing, with the coupon tester able to supply loading up to 22 kN at speeds up to 18 m/s while TMAC can supply loads of up to 500 kN at up to 8 m/s with the maximum loading somewhat inversely proportional to the test velocity. The TMAC machine is designed to test actual structural components over up to 250 mm of maximum stroke. These tests can be used to evaluate strain rate effects in materials systems from small coupons to components to in many cases actual structures. Dynamic testing as demonstrated in this work allows direct comparison of many potential approaches/combinations and provides data for design and modeling.

The TMAC machine was planned to be the main focus in demonstrating capabilities of the Mallinda resin system employed in a prototype application for direct comparison with a conventional state-of-the-art resin system commonly employed for this application. The TMAC machine was recently upgraded in part to support this project along with other requests to utilize this exclusive capability. Plans were to utilize the High Speed Tensile Tester to provide preliminary data from smaller-scale coupon tests to provide materials data for modeling purposes.

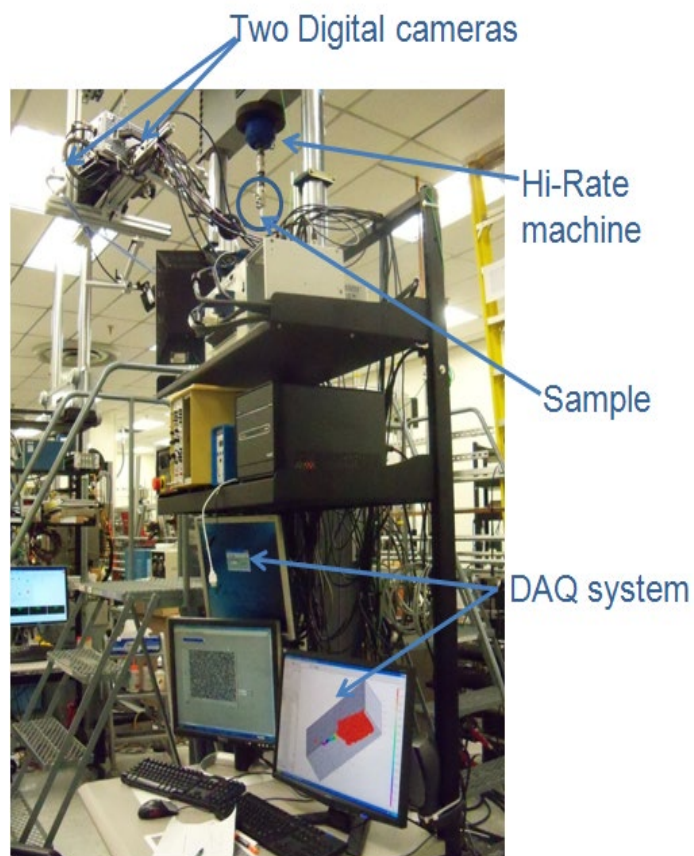


Figure 1. High Speed Tensile Tester



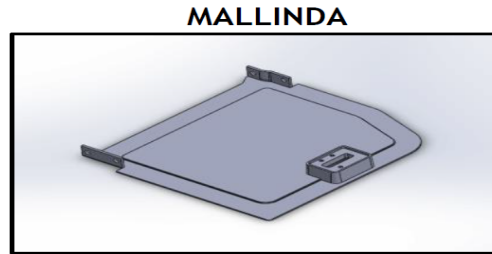
Figure 2. Test Machine for Automotive Crashworthiness (TMAC)

During this project performance period, the Mallinda team partnered with Vistex Composites to create a custom mold and carry out pilot manufacturing of the seatback component as depicted in Figure 3, which summarizes the resulting component vs. the OEM component. Original plans were for the Test Machine for the ORNL TMAC to be used in the final year of this project to evaluate the impact performance of both the OEM component and the Mallinda redesign of this component to reduce mass and take advantage of their vitrimer materials for both manufacturing and performance benefits.

Going into the concluding stages of this project, it had been much preferred that final testing focus on a full-scale demonstration in TMAC. These tests would serve to facilitate understanding of potential failure mechanisms for the actual seat back component in comparing the original design manufactured with industry standard Glass Mat Thermoplastic (GMT) materials and the newer redesign featuring state-of-the-art developmental carbon fiber in a Mallinda vitrimer matrix resin system. However, in working test details, ORNL and Mallinda determined it was going to be impractical for Mallinda to provide adequate components to do meaningful full-scale testing. In multiple discussions on how to get the most meaningful data for the investment, it was decided to test and compare the underlying materials systems in coupon form instead of more expensive and complex final components that were not available at the time. Data from the coupon tests would allow Mallinda to model, compare, and optimize the component performance utilizing the two competing material forms with more fidelity than had been possible previously. However, since the material forms being compared are so different, one being a randomly oriented glass fiber architecture as opposed to the other being a largely unidirectional carbon fiber reinforced system, the results being presented here are not directly comparable utilizing raw data alone.



- MATERIAL USED : GMT
- TOTAL VOLUME: 1600 cc
- APPROX. WEIGHT: 4.5 lbs.
- FIBER VOLUME: 45%
- NOT RECYCLABLE



- MATERIAL USED : CF-
PREPREG (MALLINDA)
- TOTAL VOLUME: 791.6 cc
- APPROX. WEIGHT: 2.5 lbs.
- FIBER VOLUME: 60%
- RECYCLABLE

Figure 3. Mallinda redesign of seatback component for manufacture using vitrimer prepreg.

The High Speed Coupon Tester had been established primarily for direct tensile testing of composite material configurations (non-unidirectional fiber architecture) where it was expected that the composite matrix system would play a significant role in material system performance. As stated previously, the desired test profile is to operate and test at constant velocity, so ORNL test engineers have designed a “slack adapter”, shown in Figure 4, which is attached to the actuator to allow test system movement to reach targeted speeds prior to engaging and loading the test specimen. In exploring alternative means to acquire data that allowed for both direct and/or indirect 1) comparison of composite material systems that were constituted vastly differently in fiber type reinforcement, fiber architecture, and composite matrix system, and 2) comparison of inherent capabilities of the different matrix systems to effectively manage energy dissipation as a function of strain rate, the ORNL team evaluated test approaches with potential to work in this existing test equipment. An earlier thought was to test in bend or flexure mode. Preliminary testing in conventional 3-point test fixtures at modest speeds as shown in Figure 5 did demonstrate potential to further expand and exploit this approach to meet most of the testing objectives



Figure 4. Slack Adapter Utilized to Allow Test Machine to Reach Targeted Speed before Engaging Specimen



Figure 5. Preliminary Testing in 3-Point Bend Test Fixture without Slack Adapter to Maintain Constant Velocity

Based largely on ASTM D790, Flexural Properties of Unreinforced and Reinforced Plastics and Electrical Insulating Materials, the test technique assumes the following:

-The relationship for the center displacement (δ) and strain (ϵ_f) on the beam outer fiber:

$$\delta = \frac{\epsilon_f}{6h} S^2 \quad [1]$$

Where S is the full span of the specimen between end supports and h is the height or thickness of the test specimen

-Taking derivatives of both sides of equation 1:

$$\dot{\delta} = \frac{\dot{\epsilon}_f}{6h} S^2 \quad [2]$$

-We now have displacement ($\dot{\delta}$) and strain ($\dot{\epsilon}_f$) rates.

-ASTM recommends S/h ratio = 40 to avoid short beam shear failure

- Initial specimens for exploration were approximately 25.4 cm (10 inches) in length and 4.6 mm (0.18 inch) in thickness, and that the span was then 18.3 cm (7.2 inches) for $S/h=40$

It was determined the fastest displacement rate to prevent fixture damage would be prescribed as ~1000 cm/sec (400 inches/sec). Therefore, subdividing the specimen thickness repeatedly, the following table was created demonstrating the relationship of testing configurations versus strain rates while maintaining the maximum velocity of 1000 cm/sec (400 in/sec), and S/h ratio of 40 as shown in Table 1.

S	h	S/h	Velocity	Strain Rate
(cm)	(mm)		(cm/sec)	/sec
18.29	4.57	40	1000	8.20
9.14	2.29	40	1000	16.40
4.57	.14	40	1000	32.81
2.29	0.57	40	1000	65.62
1.14	0.29	40	1000	131.23
0.57	.014	40	1000	262.47

Table 1. Theoretically possible strain rates at maximum velocity as a function of test configuration.

Although it was originally desirable to explore a wider range of strain rate values, it was decided for practical test specimen manufacturing and test execution that the 4.6 mm (0.180 in) thickness and 18.3cm (7.2 in) test span would be preferred to maintain constant versus other options. While this configuration and limiting the maximum displacement rate to 400 in/sec also limits the maximum strain rate to about 8.3 /sec, a general rule of thumb from earlier testing indicated that most strain rate effects of interest in automotive events are encountered at or below this strain rate level. To facilitate this testing, a new customized test fixture was designed and built as shown in Figures 6 and 7 with the slack adapter attached. A high rate, constant velocity test on this machine can only be run in tension. To achieve this, the fixture was configured with the center roller fixed and the frame with the outside rollers articulated downward. The frame is attached to the slack adapter on top of the actuator to achieve the desired velocity before engaging the specimen and starting loading.

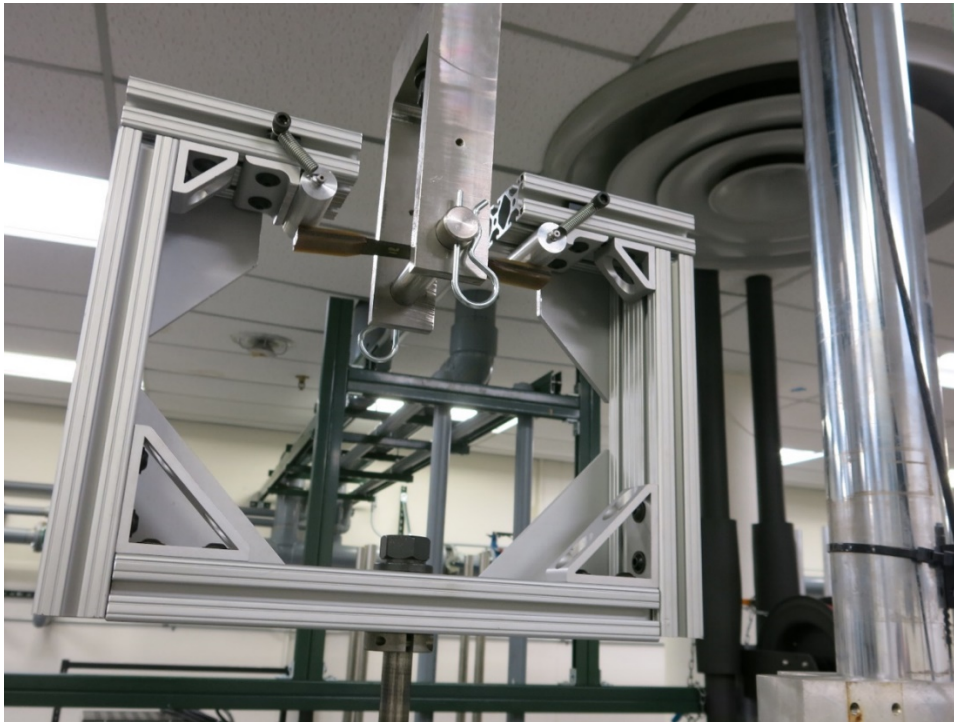


Figure 6. The High Rate Three Point Bend fixture



Figure 7. Provides a better view of the slack adapter/actuator.

The test machine has an 18 m/sec (700 in/sec) actuator with a 400 GPM servo-valve, that is driven with a 5 gallon accumulator on the pressure side. The frame has 100-kip load capacity, and the actuator has 15-inches of travel. There are two load cells, a 10-kip strain gauge cell, and a 9-kip Kistler piezoelectric cell for more rapid response. The software to control the test and drive the waveform to the MTS 407 analog controller is custom, in-house developed using LabView. Data acquisition (A/D) and control (D/A) is achieved with a National Instruments (NI) PXI chassis that is equipped with a variety of NI PXI Multi-Function input/output (I/O) cards. Synchronization was reduced to approximately 10 microseconds (slew rate of the analog conditioners) by timing the signals through the PXI chassis clock versus the computer clock.

Mallinda shipped in samples of their material and some industry standard GMT from Hanwha for comparison. ORNL set up and ran tests in the above configuration at velocities of nominally 125, 250, 500, and 1000 cm/sec (50, 100, 200, and 400 in/sec), with corresponding strain rates of approximately 1.0, 2.1, 4.2, and 8.3 /sec. Data is plotted in Figure 8 showing maximum recorded stress versus speed. Although plans were to run more samples to get more detailed test statistics, the test machine platen extensometer was destroyed during the first test at 400 in/sec. The project period of performance expired before the extensometer could be replaced and the entire planned test matrix completed. However, the data appears to show relatively small scatter and slight strain rate effects with mildly increasing stress as a function of speed for the GMT material tested both in machine direction and transverse to that direction. For the Mallinda unidirectional carbon coupons, the stress at failure was significantly higher as expected regardless of speed. However, the greater data scatter along with small number of samples prevents us from drawing firm conclusions as to failure stress as a function of speed, although it appears that there is not a significant speed effect.

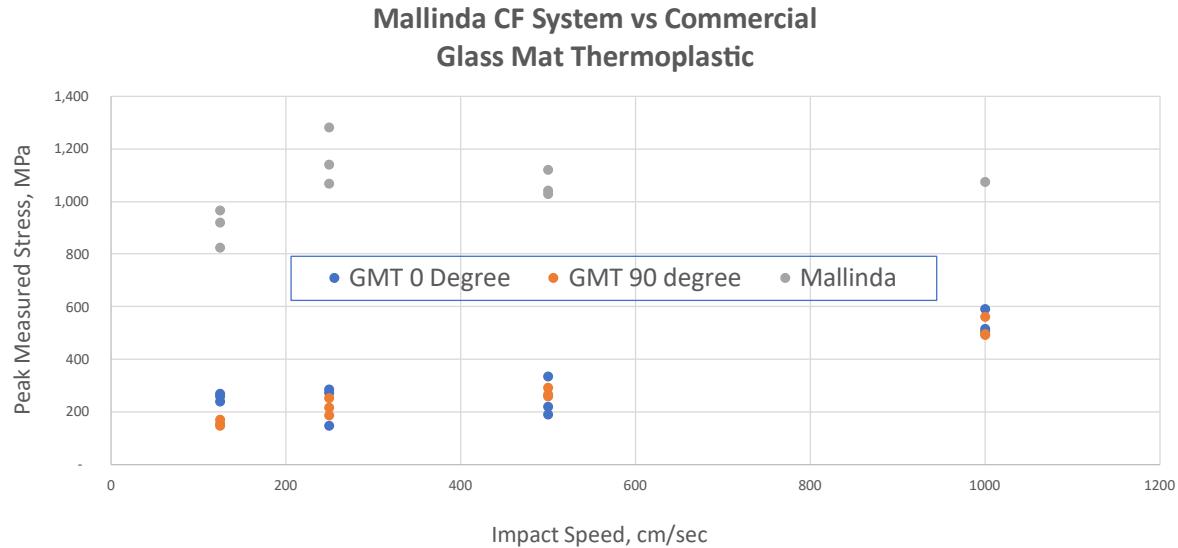


Figure 8. Dynamic test data comparing Mallinda material with commercial thermoplastic

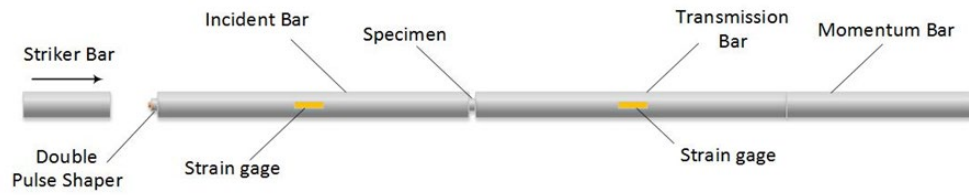
A secondary objective had been to also provide test data from high-speed tensile testing of the unidirectional carbon fiber reinforced Mallinda resin system. Since this system is unidirectionally reinforced, it was not expected that data would be strongly influenced by choice of resin system or by testing strain rate beyond factors such as fiber strength translation factor that can be obtained in static testing. However, it had been planned to obtain this data for the Mallinda system to provide input to future modeling. Based on some earlier testing, it was estimated that a sample thickness of up to a standard ASTM coupon thickness of about 0.040 in could be adequately gripped and pulled to failure using the slack adapter in the High Speed Coupon Tester configuration. However, tests were unsuccessful due to severe slippage in the grips and our funding authorization expired while the machine was down for repair of the machine Temposonics displacement measuring device.

Summary of Sandia Research Results

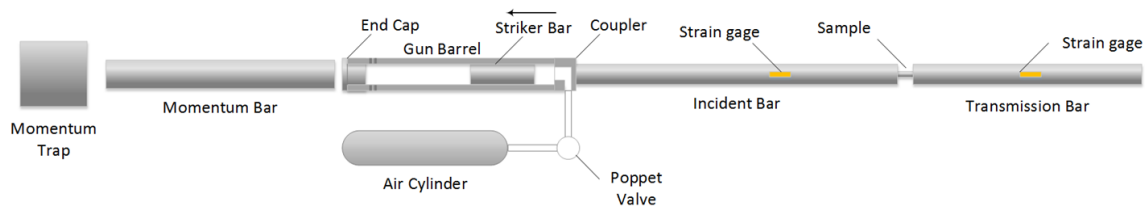
by Bo Song

In this project, Sandia conducted dynamic mechanical property characterization of Mallinda's composite materials at various strain rates in compression, tension, and three-point-bending. Both experimental and diagnostic techniques were developed for evaluation of composite materials at intermediate strain rate regime where low-speed impact, i.e., car crash, occurs. This study provides insights of material reliability and suitability for automotive applications.

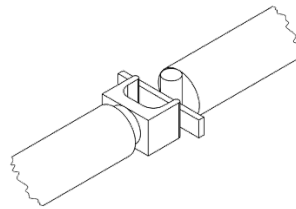
During the period of project, two carbon fiber composites (woven and unidirectional composites) were dynamically characterized. For the woven composite, dynamic compression and tension tests were conducted at different strain rates with Kolsky compression and tension bars, respectively. For the unidirectional composite, a Kolsky compression bar was used for dynamic compression and three-point-bending (TPB) tests to understand strain rate effects on the dynamic compressive stress-strain response and impact velocity effects on the dynamic flexural response, respectively. Figure 9 shows the schematics of Kolsky bar setups for dynamic compression, tension, and TPB tests. It is noted that, through this project a new diagnostic technique was developed, as illustrated in Figure 10, to simultaneously track the displacement/strain field and cracks on the top surface and two side surfaces of a composite specimen to determine the failure strength when cracks are initiated. A high-speed camera was applied to all compression, tension, and TPB tests to photograph the failure process of the composite specimens during dynamic tests.



(a) Kolsky compression bar for dynamic compression tests



(b) Kolsky tension bar for dynamic tensile tests



(c) TPB fixture attached to the Kolsky compression bar

Figure 9. Experimental setups for dynamic characterization of composites



Figure 10. Illustration of a pair of mirrors applied to the tensile specimen for simultaneously tracking cracks at top and side surfaces.

1. Woven carbon fiber composite

Dynamic compression tests were conducted on the woven composite along in-plane (the loading direction is parallel to the plane of woven fabric; $\sim 45^\circ/135^\circ$ to the fiber direction) and out-of-plane (the loading direction is perpendicular to the plane of woven fabric). The compressive stress-strain curves are shown in Figure 11. As also seen in Figure 11, the woven composite exhibits very little strain rate effect on the compressive stress-strain response within the strain rate range conducted in this study. The dynamic compressive stress-strain response along in-plane direction is quite different from that along out-of-plane direction. The stress-strain curves of the composite along out-of-plane direction are more linear and with higher failure strength and strain than those along in-plane direction. The significant anisotropy of the composite along in-plane and out-of-plane directions also leads to different failure mode, as shown in Figure 12. The in-plane specimen failed via splitting; whereas the out-of-plane specimen catastrophically failed.

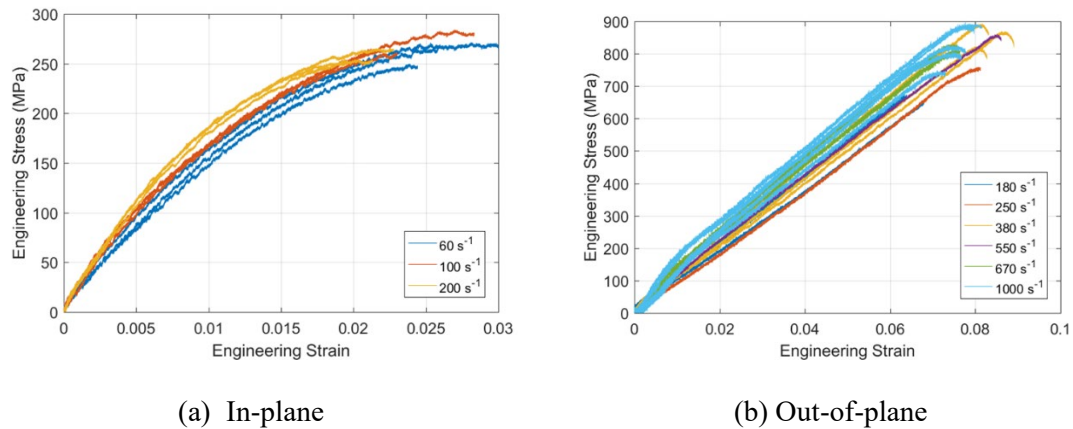


Figure 11. Dynamic compressive stress-strain curves of woven composites at various strain rates.

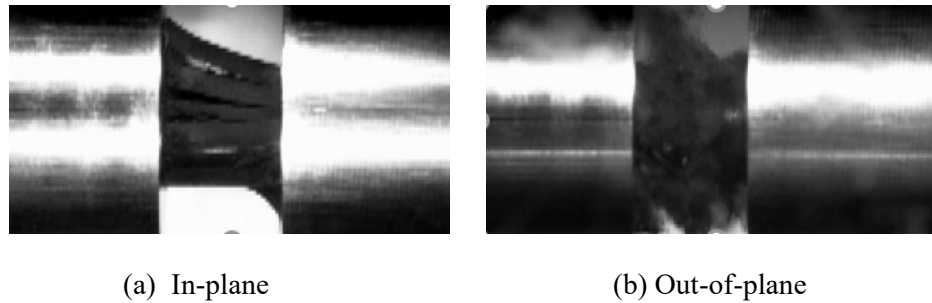


Figure 12. Failure mode of the woven composite during dynamic compression

Figure 13 shows the dynamic tensile stress-strain response the woven composite. The tensile load was parallel to the fabric (in-plane). The dynamic tensile stress-strain curves are similar to the compressive stress-strain curves shown in Figure 11(a). The results from the high-speed imaging with digital image correlation (DIC) show that the crack was initiated prior to the peak load, as shown in Figure 14.

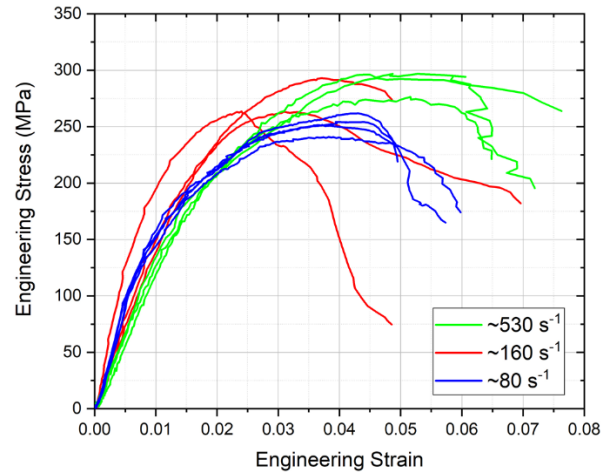


Figure 13. Dynamic tensile stress-strain curves of woven composite.

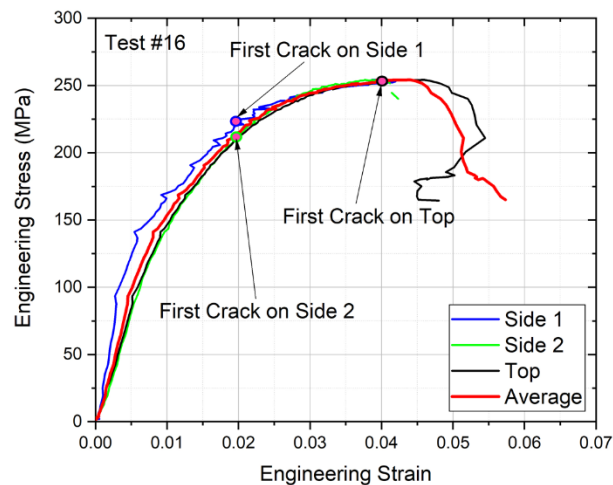


Figure 13. Crack initiation observed on the top and both side surfaces during dynamic tension.

2. Unidirectional carbon fiber composite

The dynamic compressive characterization of the unidirectional carbon fiber composite followed the same testing procedure as that for the woven composite. For the in-plane direction, the loading direction is parallel to the fiber direction (0°). Figure 14 shows the dynamic stress-strain curves along the in-plane and out-of-plane directions. The material along the in-plane direction showed a higher modulus but lower failure strength and strain than those along the out-of-plane direction. The strain-rate effect along both directions are insignificant. As shown in Figure 15, under dynamic compression, the material along in-plane direction showed a failure mode of splitting; whereas, the material along out-of-plane direction showed a shear failure mode.

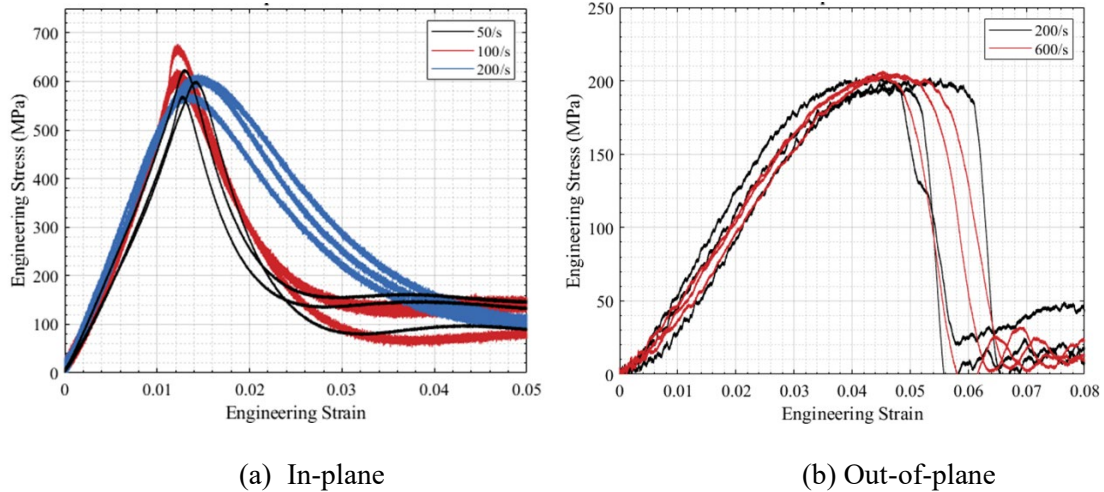


Figure 14. Dynamic compressive stress-strain curves of unidirectional composite.

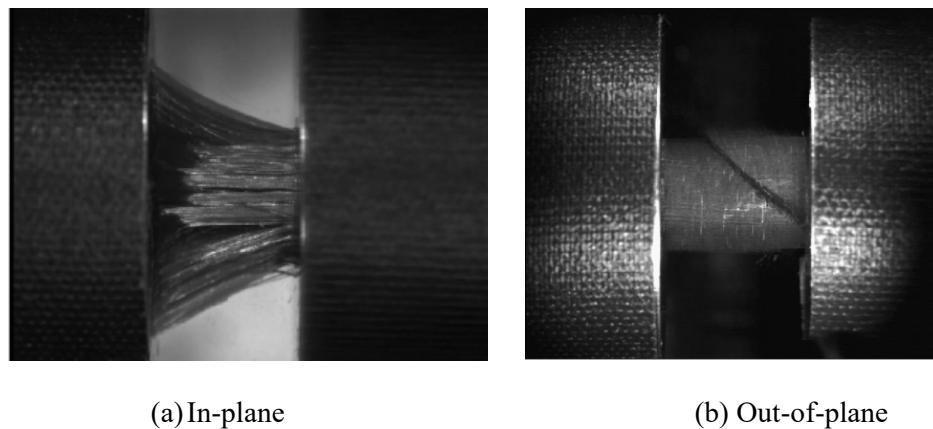
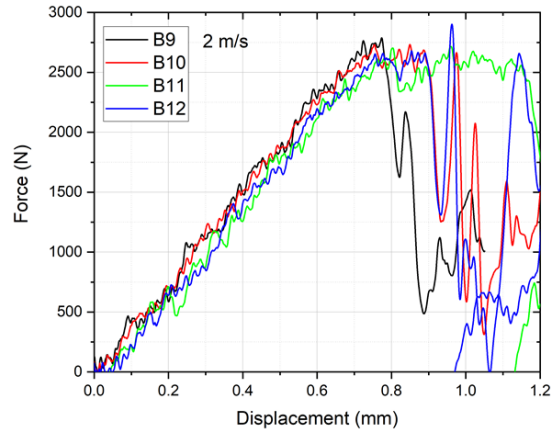
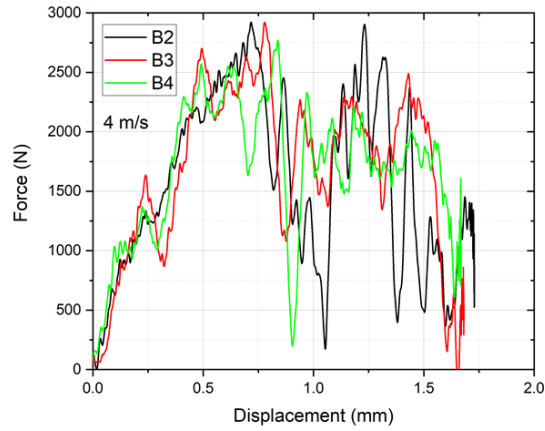


Figure 15. Failure mode of the unidirectional composite under dynamic compression.

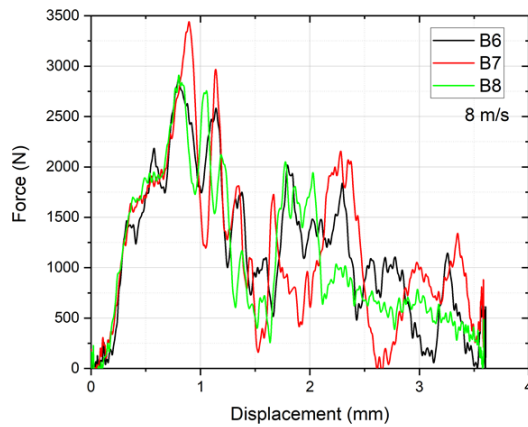
Dynamic TPB tests of the unidirectional composite was conducted with the same Kolsky compression bar with the fixture shown in Figure 9(c). The length direction of the beam specimen aligns with the fiber direction. The force-displacement curves from the TPB tests at various impact velocities are shown in Figure 16. The flexural stress-strain curves at the back side of the beam specimen were also calculated and shown in Figure 17. Figures 16 and 17 show that the maximum force and flexural stress were independent of impact velocity or strain rate. However, the flexural modulus was observed to be impact velocity (or strain rate) dependent, as shown in Figure 18. Under dynamic TPB, the composite beam specimen was failed via delamination first and then tensile failure with increased load, as shown in Figure 19.



(a) 2 m/s

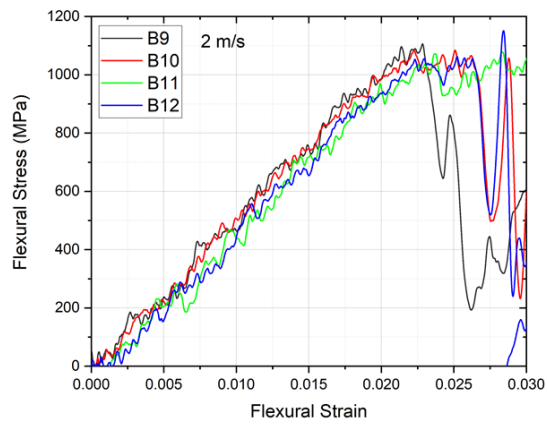


(b) 4 m/s

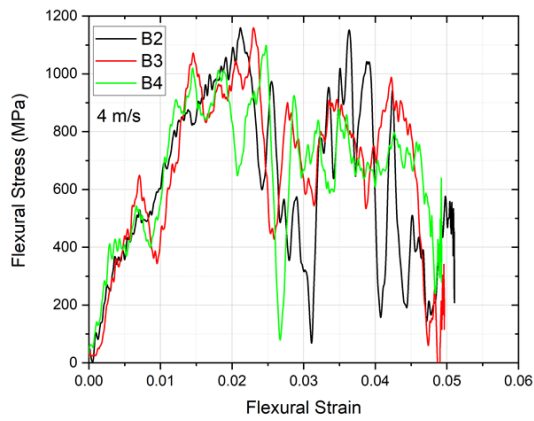


(c) 8 m/s

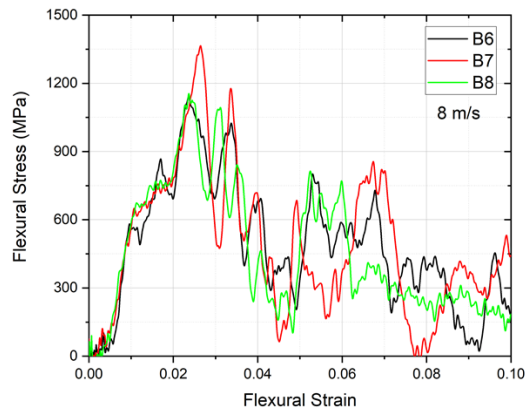
Figure 16. Force-displacement curves from the TPB tests.



(a) 2 m/s



(b) 4 m/s



(c) 8 m/s

Figure 17. Flexural stress-strain curves from the TPB tests.

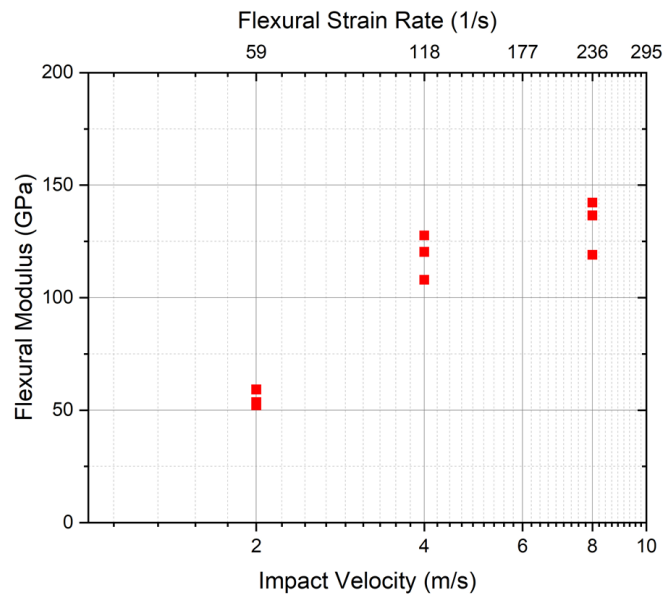


Figure 18. Effect of impact velocity (strain rate) on flexural modulus.

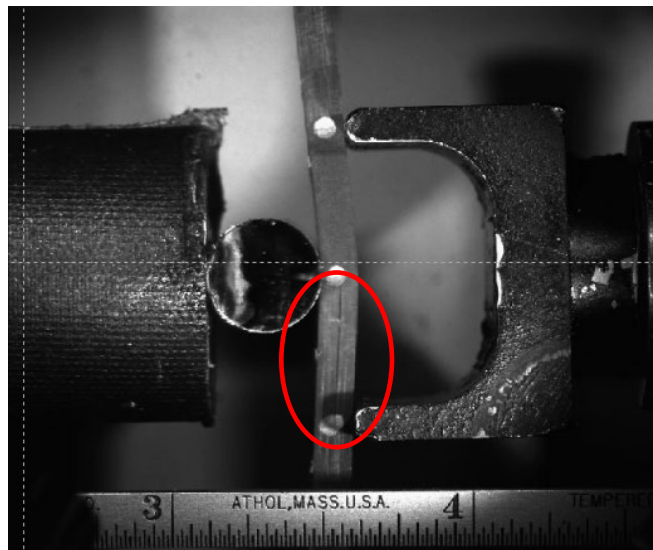


Figure 19. Composite beam specimen failure under dynamic TPB.

Summary of PNNL Research Results

by Michael Larche, Lisa Fring, Matt Prowant, Michael Hughes, and Leo Fifield

Introduction

The recent development of a malleable thermoset composite system requires extensive validation through testing to support the industry acceptance of this technology. Mallinda has demonstrated the manufacturability of its resin through prepreg production trials, and the testing of this material utilized the capabilities at three of the national laboratories. The Pacific Northwest National Laboratory (PNNL) was tasked with characterizing microscopic defects in cured panels using ultrasonic analysis. This was followed by destructive analysis to image the defects and validate the ultrasonic findings.

Materials

The Mallinda team submitted two sets of flat panels to PNNL for ultrasonic characterization, along with one scoping panel to allow for ultrasonic test setup and method validation. All panels were fabricated at the Mallinda facility and were approximately six inches by six inches in size. The first set was submitted to PNNL in November 2020, and Table 2 below summarizes the processing parameters used for each panel. Panel 0 in the Table is the scoping panel.

Table 2: Process Parameters for Panel Set #1

Panel	Ply Count	Cure Temp (C)	Cure Time (min)	Consolidation Temp (C)	Consolidation Time (sec)	Consolidation Pressure (psi)	Edge Condition
0	7			180	300	700	Trimmed
1	12	115, 150, 180	60, 40, 20	180	600	400	Trimmed
2	12	115, 150, 180	60, 40, 20	200	300	200	Trimmed
3	12	115, 150, 180	60, 40, 20	180	30	400	Trimmed
4	12	115, 150, 180	60, 40, 20	200	60	100	Trimmed
5	12	115, 150, 180	60, 40, 20	160	30	100	Trimmed

Representative pictures of the scoping panel and one of the test panels from panel set #1 are shown in Figure 20 below.

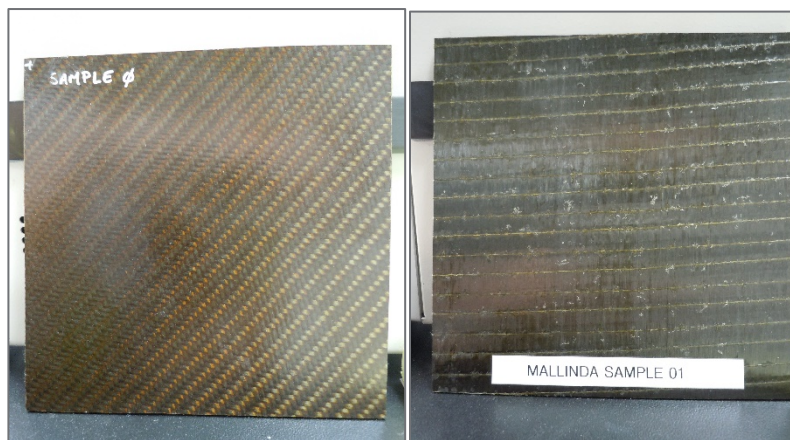


Figure 20: Test panels submitted for ultrasonic analysis from set #1

The second set of panels was submitted to PNNL in May 2021. Table 3 below summarizes the processing parameters used for each panel. These panels were sealed by Mallinda on the top and bottom surfaces and on all edges. Rust-oleum ultra cover gloss clear was used to seal the top and bottom surfaces, and silicone was used to seal the edges.

Table 3: Process Parameters for Panel Set #2

Panel	Ply Count	Cure Temp (C)	Cure Time (min)	Consolidation Temp (C)	Consolidation Time (sec)	Consolidation Pressure (psi)	Edge Condition
1	12	115, 150, 180	60, 40, 20	180	60	400	Trimmed and sealed
2	12	115, 150, 180	60, 40, 20	200	300	200	Trimmed and sealed
3	12	115, 150, 180	60, 40, 20	200	60	100	Trimmed and sealed

Representative pictures of the test panels from set # 2 are shown below in Figure 21.

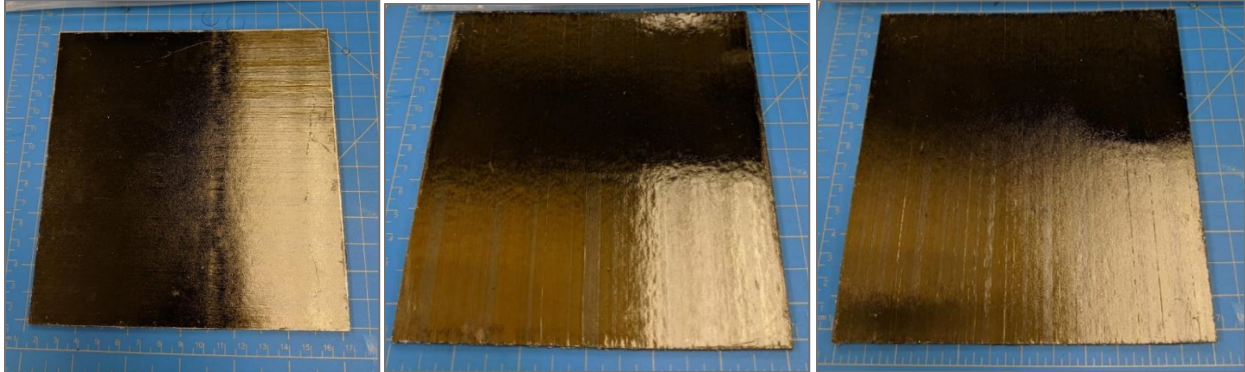


Figure 21: Pictured left to right, Panel 1, Panel 2, and Panel 3 from set #2 in as-received condition

Ultrasonic Analysis Method

Plates were inspected using a focused ultrasonic immersion probe at 10 MHz. The probe used for interrogation of the samples was 0.5” diameter with a 1” focal distance, and standoff was set at that focal distance to the front surface of the plate. To ensure equilibrium in the water, each plate was immersed for 24 hours prior to scanning, and no sample was left in the water longer than 36 hours. The scanning setup is shown in Figure 22.

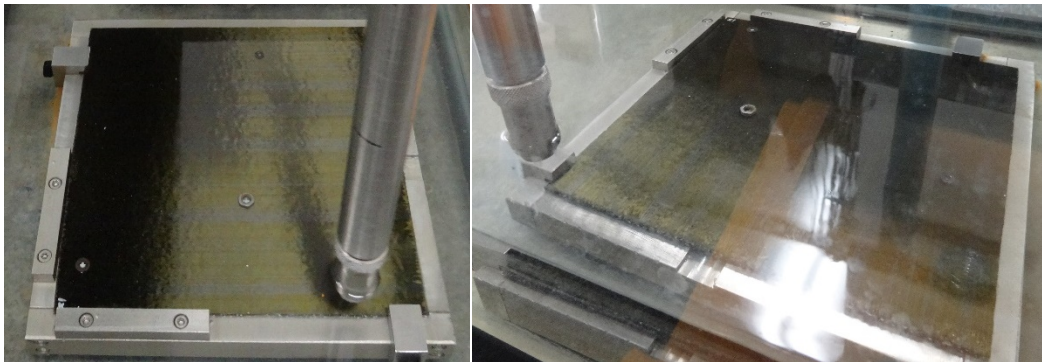


Figure 22. Immersion scanning configuration

Each plate was aligned to the scanner and held in place using a fabricated steel fixture and scanning was performed in a 3x3 grid of files, each collected at 0.5 mm resolution with 3 mm of overlap on boundaries. Data was collected at 2 GS/s over a 4-5 μ s window gating the signal response of the plate. Three unique fiducials were placed on each plate, visible in Figure 22, at known locations to ensure correct reconstruction of the data images for processing. An example of the resulting raw data image is shown in Figure 23.

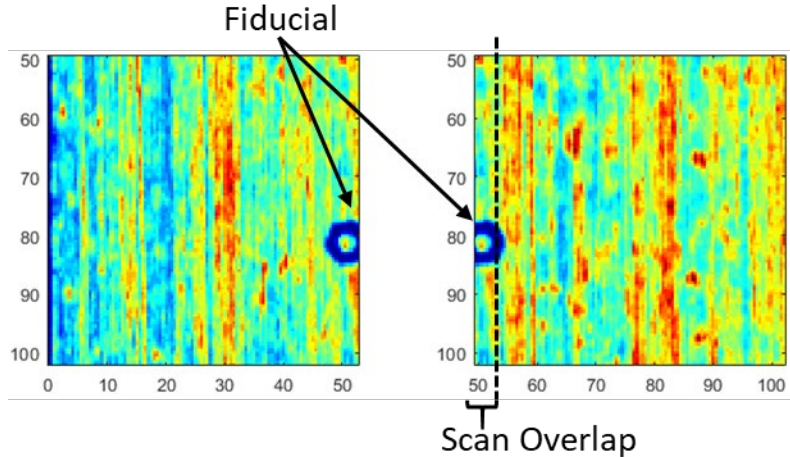


Figure 23. Two raw data C-scans, showing overlap and a fiducial

Many studies have demonstrated the utility of different entropies for detection of subresolution backscattering structures in both materials characterization and medical ultrasonics. Frequently, these techniques detect changes that are not detectable by other approaches. These include reliable detection of near-surface defects, diffuse accumulation of subwavelength-sized nanoparticle-based ultrasound contrast agents [1-5]. PNNL has recently applied several entropies, defined below, to extend previous results on the detection of foreign objects in graphite/epoxy composites [6].

All RF data were obtained by sampling a continuous real function, $y = f(t)$, which is the backscattered waveform. PNNL employed the convention that the domain of $f(t)$ is $[0,1]$, and always assumed that underlying all of the digitized signals is a function that is differentiable. PNNL also assumed that $f(t)$ is Lebesgue measurable so that it has a distribution function $y = w_f(t)$. Roughly, $w(y)$ indicates how often $f(t) = y$.

$$\log[E_f] = \log \left[\int_0^1 f(t)^2 dt \right]. \tag{1}$$

We may also compute Shannon's entropy, which for continuous signals $f(t)$ (sometimes also referred to as the differential entropy[7]) is given by

$$H_f = \int_{f_{min}}^{f_{max}} w_f(y) \log[w_f(y)] dy, \tag{2}$$

In several studies H_f has demonstrated sensitivity to subtle changes in scattering architecture[8].

If $f(t)$ is differentiable, then $w_f(y)$ may be computed using

$$w_f(y) = \sum_{\{t_k | f(t_k)=y\}} \frac{1}{|f'(t_k)|} \tag{3}$$

At this point it is worth emphasizing since $f(t)$ is Lebesgue measurable, it constitutes a “bona fide” random variable. Hence, the approach is a special case of statistical signal processing. However, since the functions considered are also differentiable, the distribution functions of the random variables are directly accessible

from the functions themselves via the equation above. In the general situation this is not true as most random variables are nowhere differentiable, since the set of differentiable functions in $C^1[0,1]$ has Wiener measure zero.

The most useful entropy found is a generalization of joint entropy of two random variables to the case where those variables are differentiable. In this regime the joint distribution, $w_{f,g}(x,y)$ for two random variables $x = f(t)$ and $y = g(t)$, written more simply as $w_{f,g}(x,y)$, becomes a “singular” mathematical object roughly analogous to a series of Dirac delta functions concentrated on the planar curve $(f(t), g(t))$. The precise object representing $w_{f,g}(x,y)$ is a Laurent distribution[9]. The limiting value of the joint entropy where dynamic range is infinite, or conversely the system resolution, ϵ , becomes zero, is itself infinite. Nevertheless, in this limit the joint entropy may be written as $\log[\epsilon] + H_{f,g}$, where $H_{f,g}$ is bounded and expressible directly in terms of $f(t)$ and $g(t)$ and their derivatives. Specifically, for backscattered radio frequency waveforms, $f(t)$, and a reference function, $g(t)$, in the case where $f(t), g(t)$ are differentiable functions this finite part, is [10]

$$H_{f,g} \equiv -\frac{1}{2} \int_0^1 dt \frac{\min[|f'(t)|, |g'(t)|]}{\max[|f'(t)|, |g'(t)|]} - \int_0^1 dt \log[\max[|f'(t)|, |g'(t)|]], \quad 4$$

which, as shown elsewhere, is well-defined even in the case where one or both of $f'(t), g'(t)$ are zero[10].

A good choice for the reference waveform, $g(t)$, is frequently the reflection from a stainless-steel plate of the emitted pulse from the insonifying transducer. However, it is possible to significantly improve upon this as described in[11].

Ultrasonic Analysis Results

All specimens were scanned in nine slightly overlapped regions 53 mm by 53 mm on a grid of 106 x 107 points (with 0.5 mm step size). At each point in the scan one hundred, 259-point (each point comprised of a 16-bit word) waveforms were acquired with a single-shot sampling rate of 2GHz, averaged, and stored for off-line analysis both, joint entropy, $H_{f,g}$ (Eq. 4), and signal energy, E_f (Eq. 1), analysis. The reference trace was generated using a reflection from the upper left corner of specimen SB01 as described in reference [11].

Figure 24 shows, from left to right, the resulting joint entropy images. Each is comprised of nine sub-images produced using the nine sub-scans acquired as described above. The overlap region has not been edited from the image to enable inspection for possible edge effects. Inclusion of the overlap regions is evident from the apparent double imaging of certain features such as the brass nut placed on top of the composite plate during scanning to produce a fiducial marker to orient scan images relative to the physical plate. It is remarked that no edge effects are observable in the composite image.

Figure 25 shows the corresponding signal energy images.

It is observed that the images are essentially the same up to inversion of the gray-scale lookup tables used to produce each image. Moreover, these images do not exhibit the usual cross-hatching pattern that has been observed in all previous studies of graphite/epoxy composited[8, 10-13]. The reasons for this are unclear. However, inspection of the raw RF, resulting in exclusion of the front and backwall echoes indicates that the image structure is generated by the internal scattering architecture of the specimens. We remark also that this behavior differs drastically from specimen (SB0 – not shown), which has the expected scattering behavior of a well-consolidated graphite/epoxy specimen and which seems to have been fabricated using different techniques than those used to manufacture SB01-SB03.

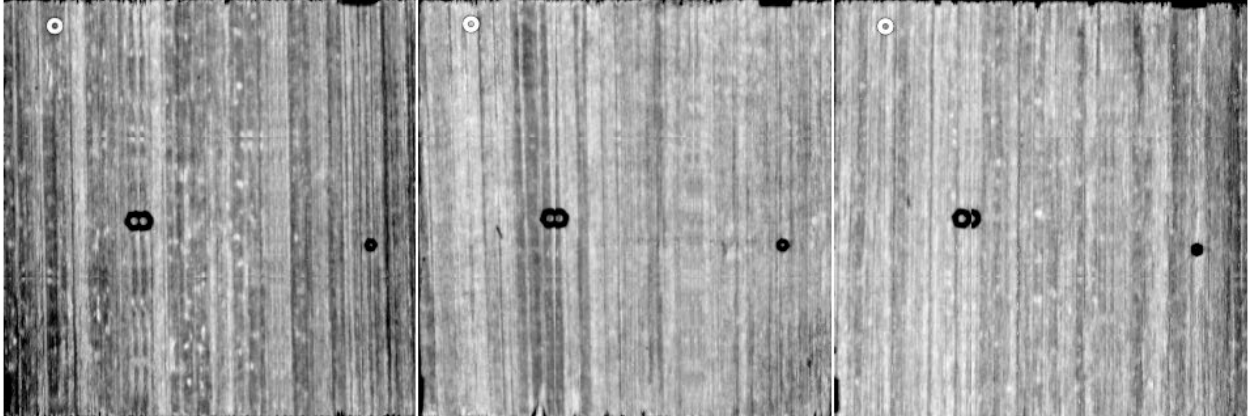


Figure 24. A joint entropy image of all three specimens in this study: From left to right: $H_{f,g}$ images for specimens SB01, SB02 and SB03

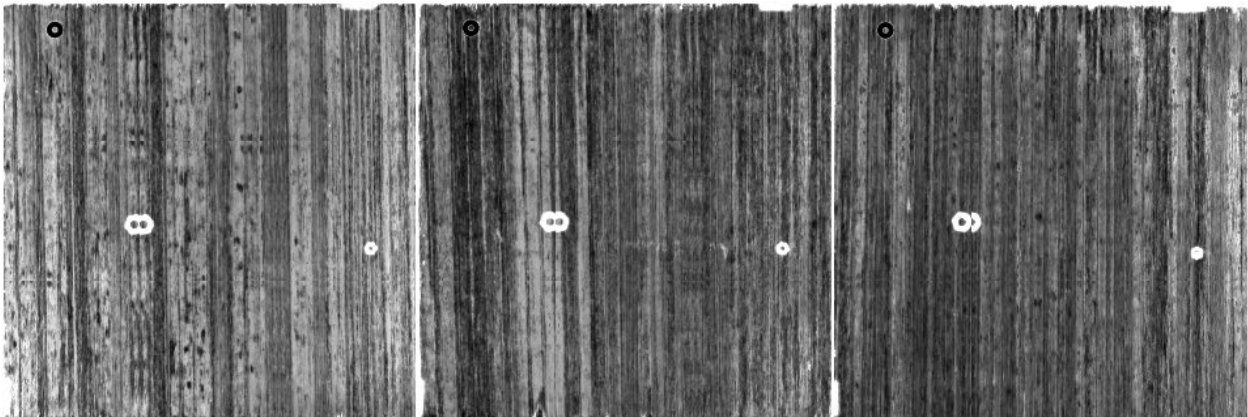


Figure 15. A joint signal energy image of all three specimens in this study: From left to right: $H_{f,g}$ images for specimens SB01, SB02 and SB03

Microscopy Method

Upon completion of the ultrasonic analysis, any indications found during scanning were marked on each panel with a silver sharpie. Half of each panel was shipped back to Mallinda, and half was submitted for microscopy cross-section analysis at PNNL.

The panels were sectioned perpendicular to the fiber direction at locations of scanning indications, as marked. Low magnification images were taken to obtain an overview of the panel consistency, and higher magnification images were taken in areas of interest.

Specimens were mounted in Buehler Epothin 2 Epoxy with a blue mount die, as shown in Figure 26. Polishing of each specimen included the following steps:

1. Plane ground sample through 1200 grit SiC paper using water
2. Intermediate polished sample(s) on 6 micron water based diamond using a Struers MD-Pan pad, 25N/sample, 150 rpm head/platen co rotate for 5-8 min.
3. Polished on 3 micron water based diamond using a Struers MD-Mol pad, 25N/sample, 150 rpm head/platen co rotate for 5 min.
4. Polished on 1 micron water based diamond using a Pace Technologies "Microcloth pad, 15 N/sample, 150 head/platen co rotate for 5 min.

5. Final polished on 0.05 micron alumina slurry using a Pace Technologies Microcloth pad, 15 N/sample, 150 head/platen co rotate for 5 min.
6. Washed in between steps with cotton ball and rinsed with ethanol, air dried.

Images were taken at several different magnifications on an Olympus BX51 optical microscope with a DP74 camera.



Figure 26: Representative image of the mount used for cross-section analysis

Microscopy Results

Panel set #1 was not evaluated because of water ingress issues encountered during the ultrasonic scanning. These panels were sent back to Mallinda for further investigation. This was a deviation from the original project plan.

The cross-section maps for the three panels from set #2 are shown below in Figures 27-29. The white dots seen in the pictures correlate to the indications found in ultrasonic analysis. Panel 2 had no indications, so cross-sections were taken across the width of the panel to capture overall consistency and architecture of that panel.

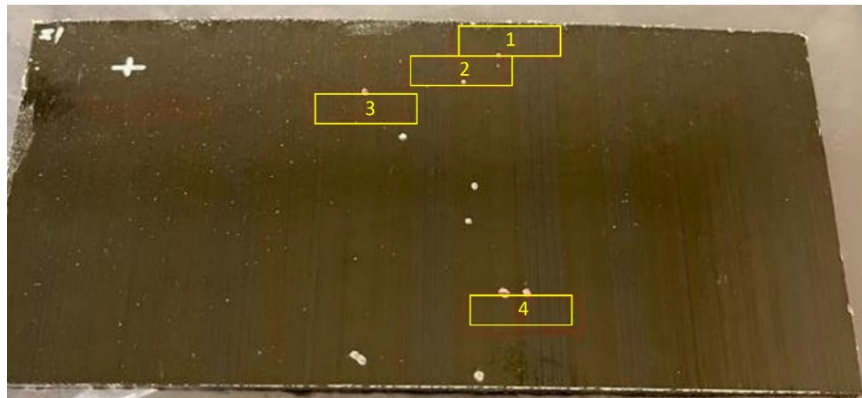


Figure 27: Picture showing where cross-sections were taken on half of panel 1 from set #2



Figure 28: Picture showing where cross-sections were taken on half of panel 2 from set #2

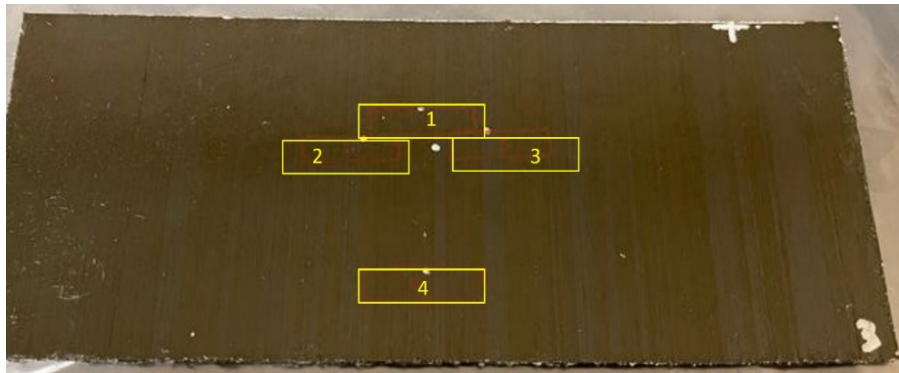


Figure 29: Picture showing where cross-sections were taken on half of panel 3 from set #2

The cross-section images of panel 1 are shown in Figures 30-33. While the interply resin region is relatively consistent in thickness in most areas, several areas of fiber waviness and inconsistent fiber bundle spread can be seen throughout all sections. There are also regions of porosity or lack of fiber impregnation present in all sections. In sections 1 and 2 this is mainly observed in the center region, correlating to the location of the ultrasonic indication. Section 2 also contains a resin rich area in the center-left area that is approximately 0.8 mm by 0.2 mm. It is not immediately clear what features in section 3 and 4 correlate to the ultrasonic indications as there are several areas that exhibit either resin richness or porosity within the fiber bundles. A few areas of resin cracking are also present in all sections from panel 1. A representative image of this cracking from panel 1 is shown in Figure 34.

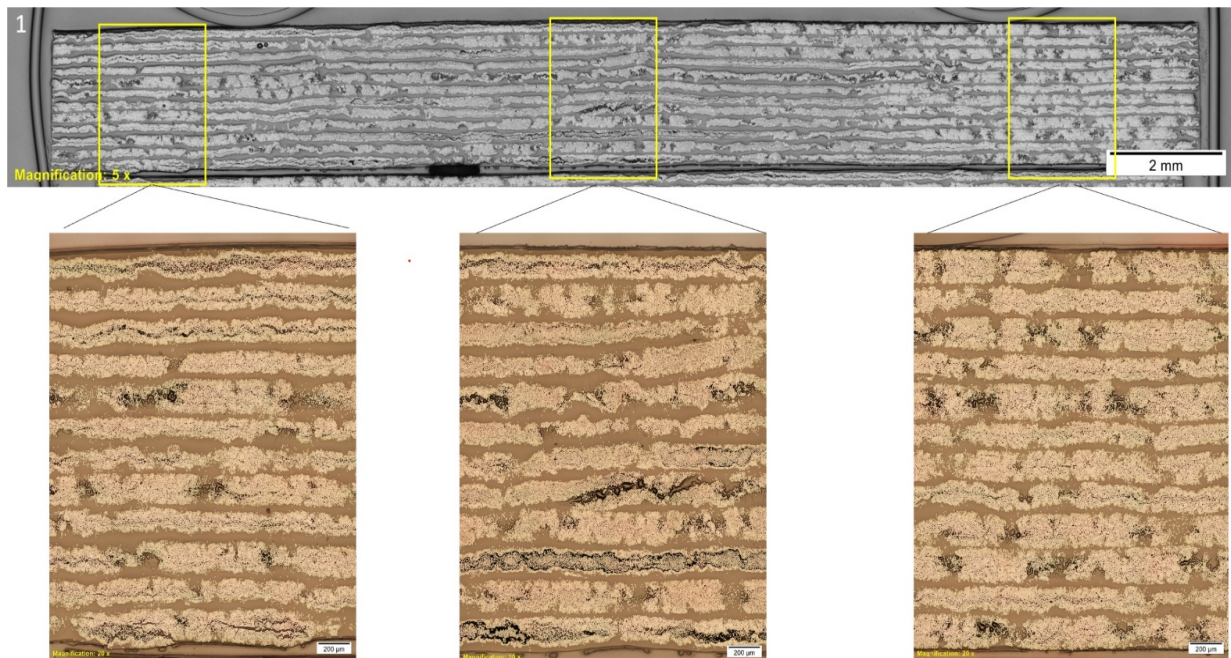


Figure 30: Panel 1, Section 1 low magnification view and high magnification view of left, center, and right areas

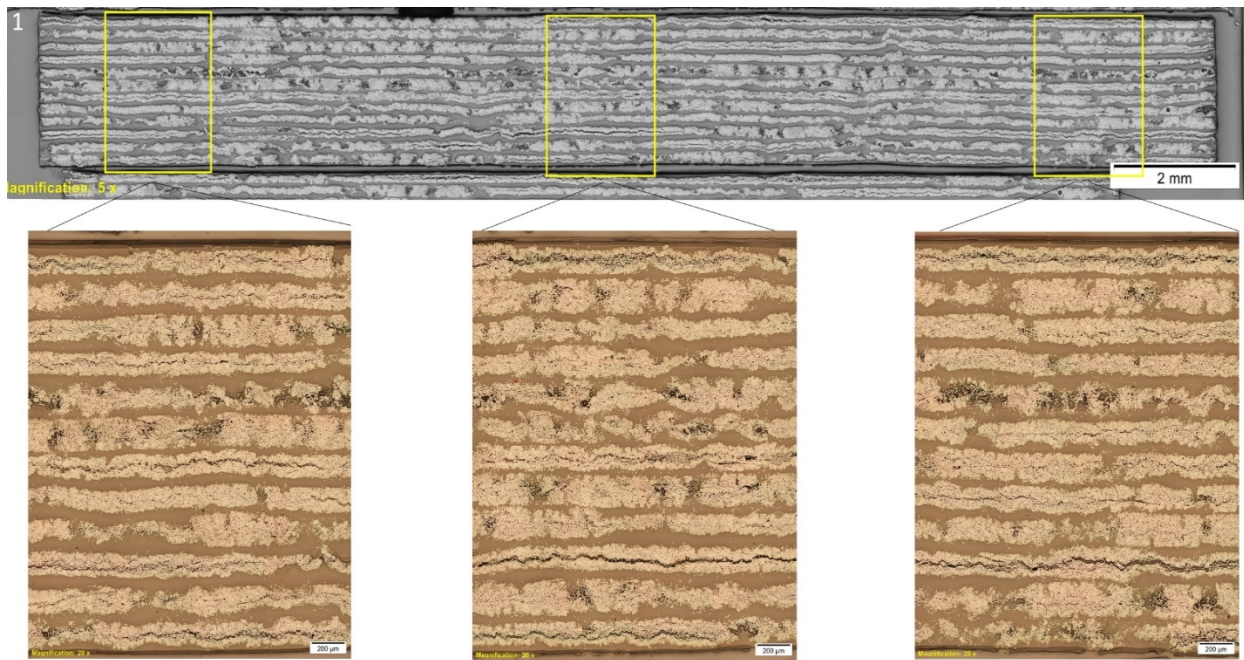


Figure 31: Panel 1, Section 2 low magnification view and high magnification view of left, center, and right areas

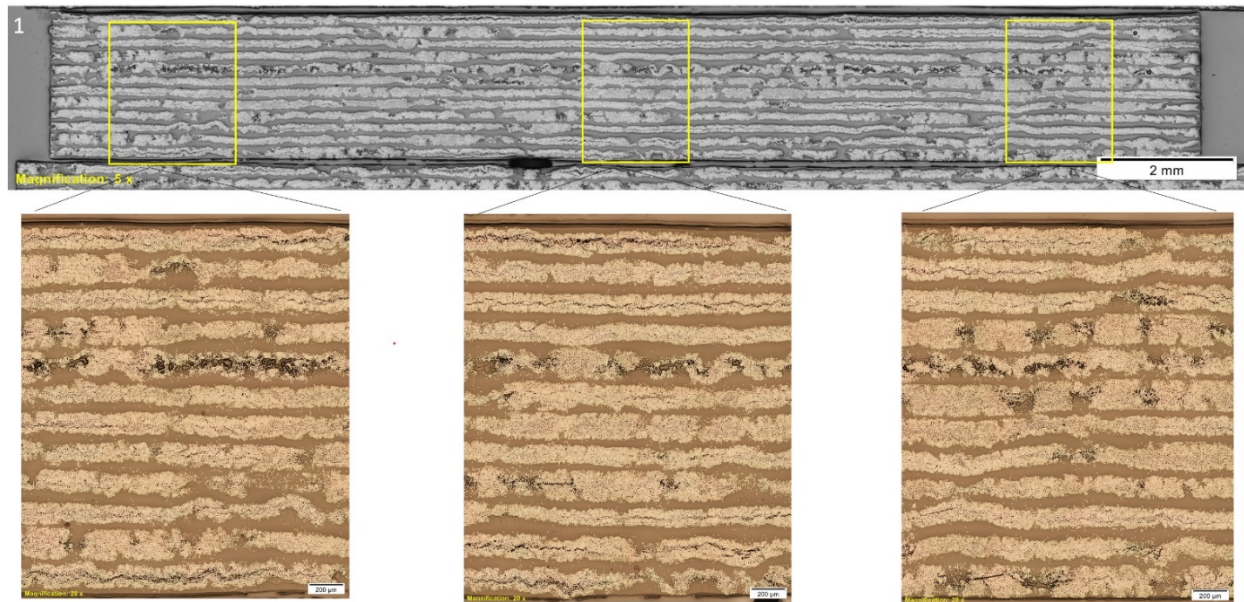


Figure 32: Panel 1, Section 3 low magnification view and high magnification view of left, center, and right areas

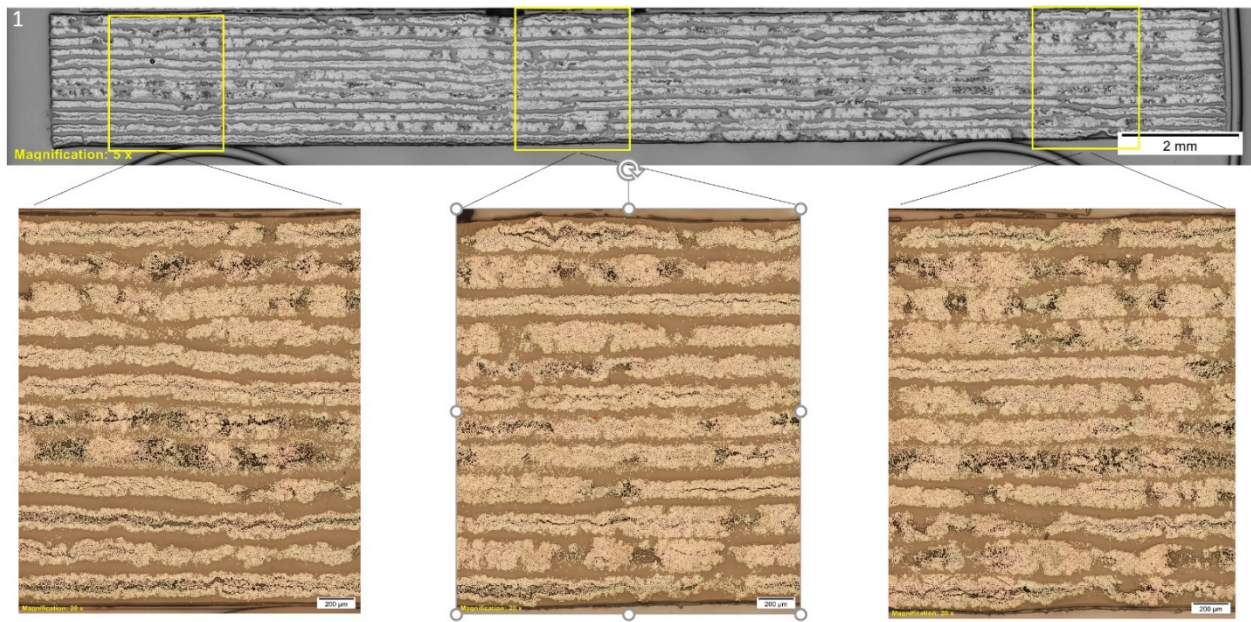


Figure 33: Panel 1, Section 4 low magnification view and high magnification view of left, center, and right areas

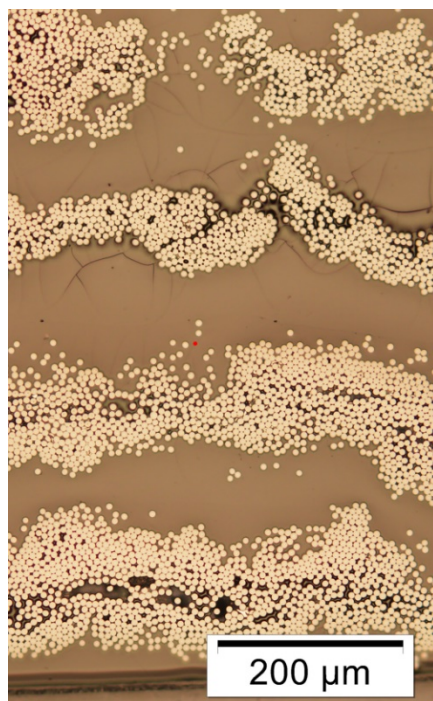


Figure 34: Example of resin cracking observed in panel 1

The cross-section images of panel 2 are shown in Figures 36-39. Panel 2 shows a region in each section where multiple, adjacent plies show interply resin thinning, as shown below in Figure 35. Similar to panel 1, but to a lesser degree, there are areas of fiber waviness, inconsistent fiber bundle spread, and porosity or lack of fiber impregnation present in all sections. Resin cracking is most pronounced in panel 2, and a representative image is shown in Figure 40. No ultrasonic indications were found in panel 2.

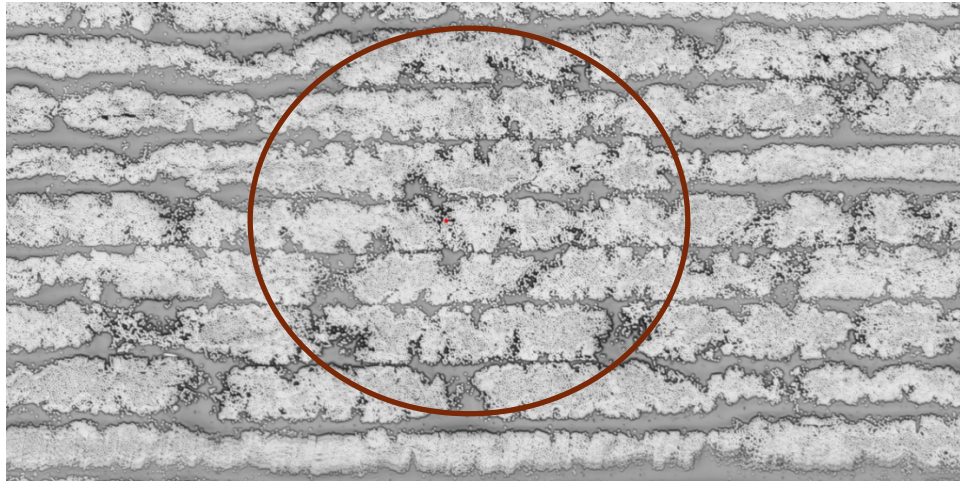


Figure 35: Image showing area of interply resin thinning

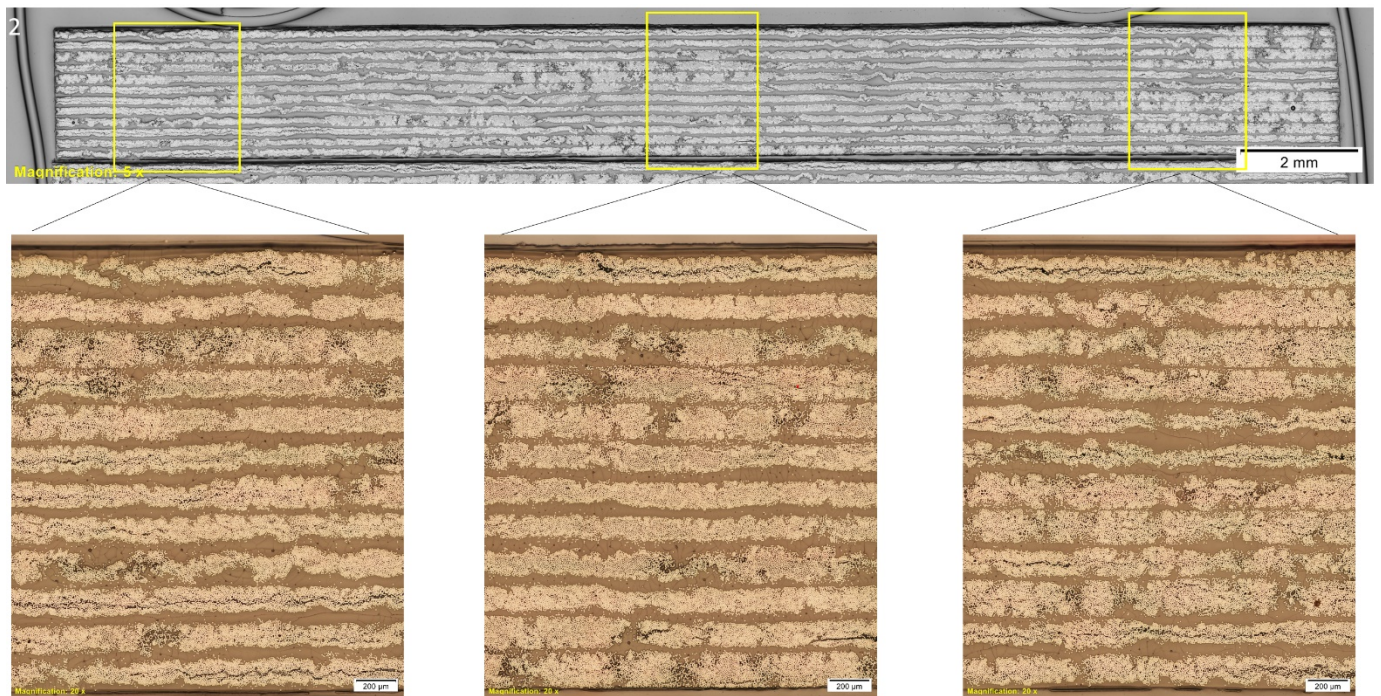


Figure 36: Panel 2, Section 1 low magnification view and high magnification view of left, center, and right areas

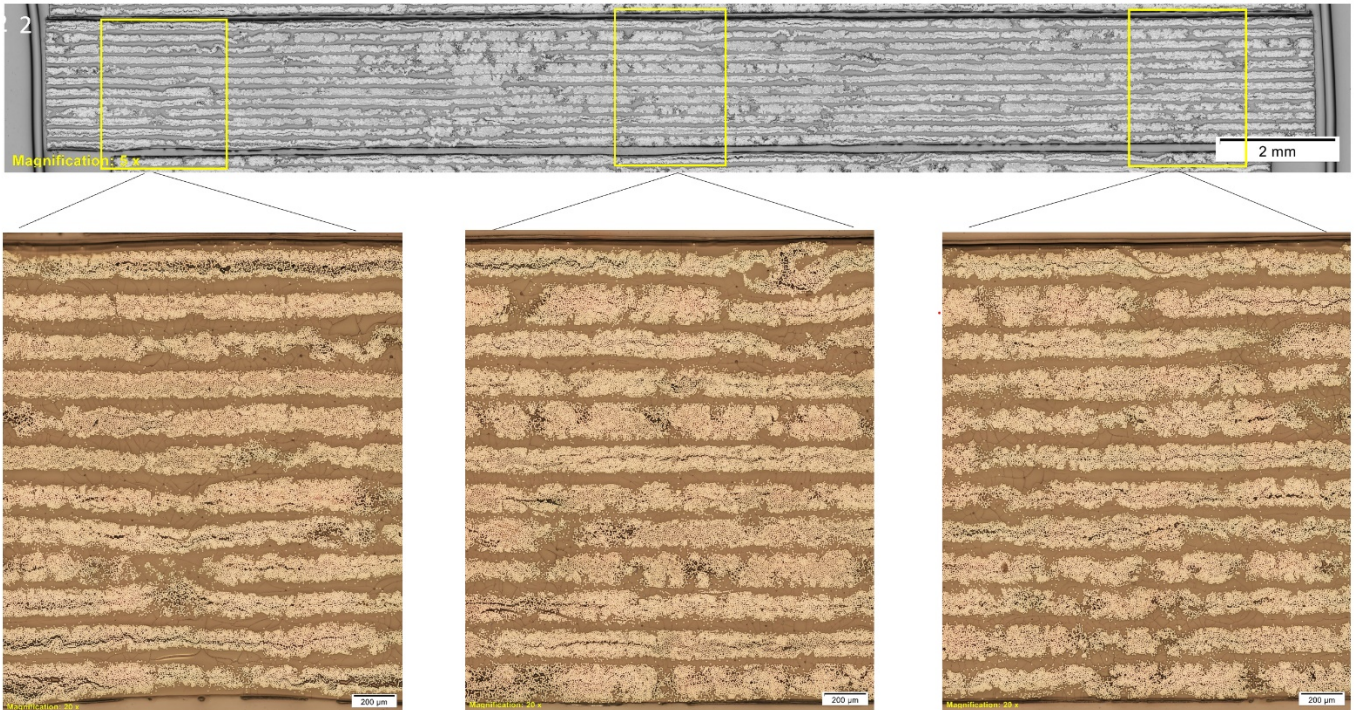


Figure 37: Panel 2, Section 2 low magnification view and high magnification view of left, center, and right areas

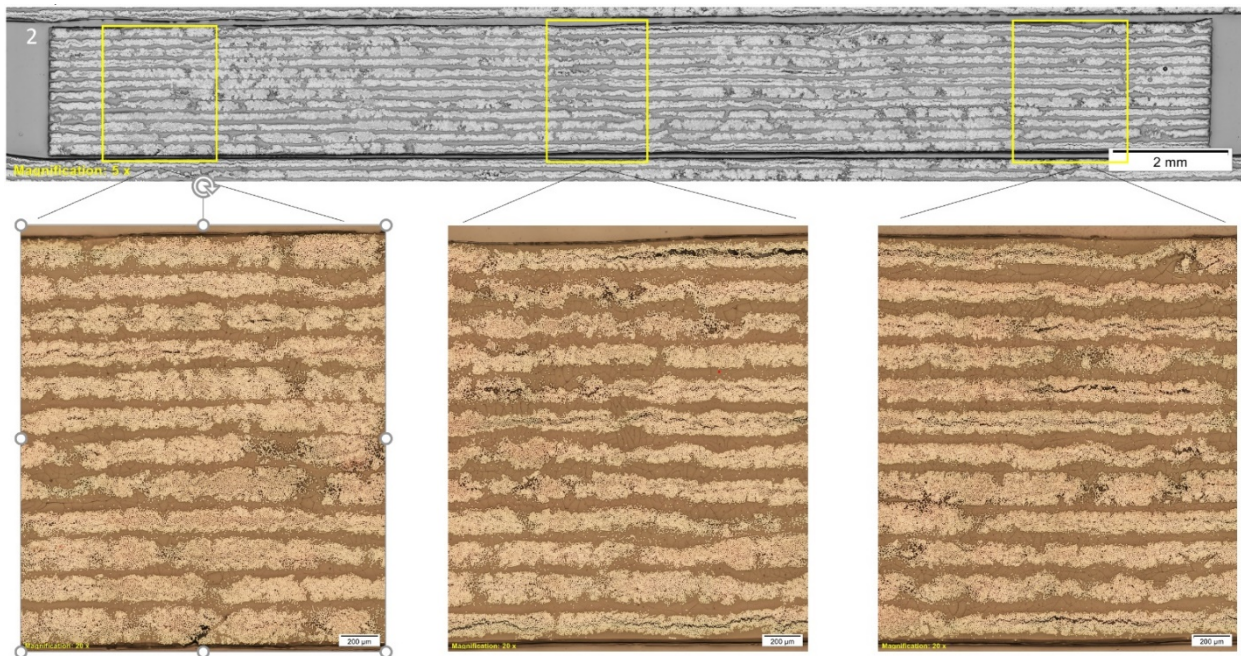


Figure 38: Panel 2, Section 3 low magnification view and high magnification view of left, center, and right areas

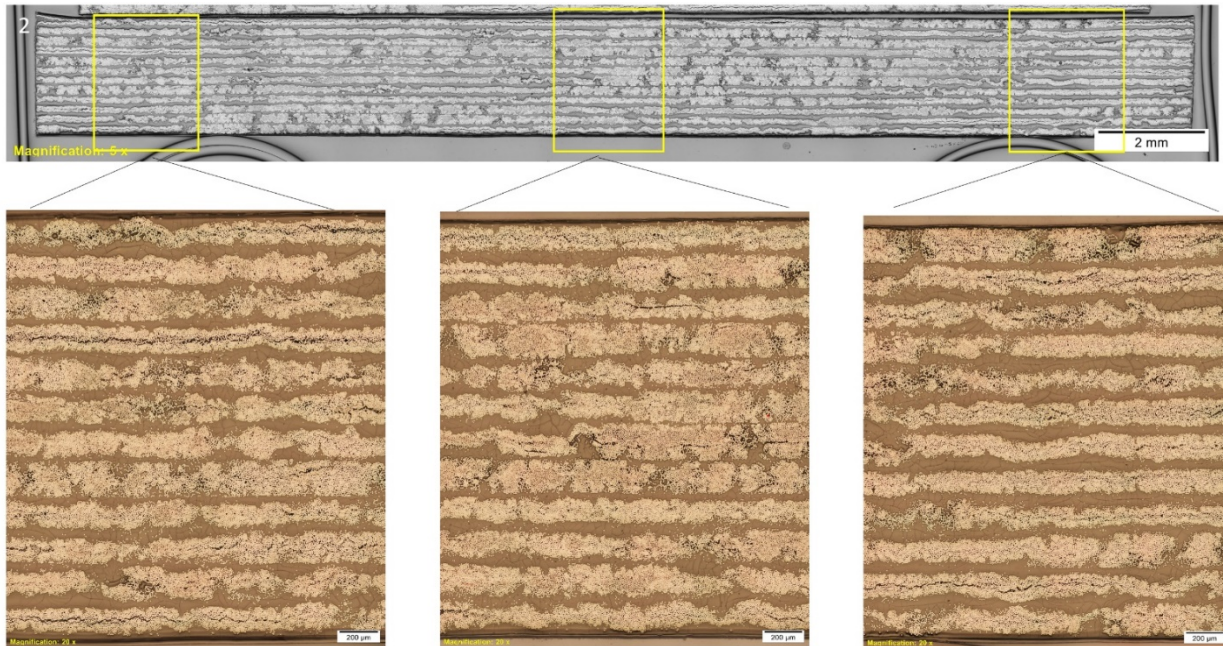


Figure 39: Panel 2, Section 4 low magnification view and high magnification view of left, center, and right areas

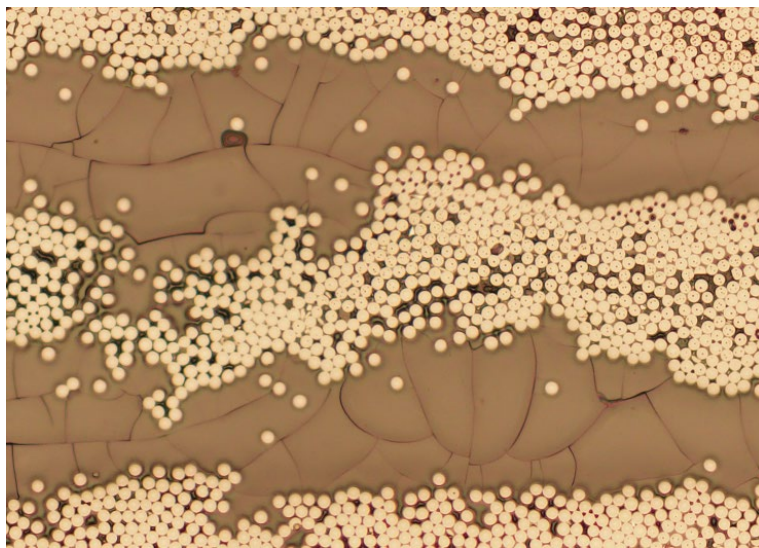


Figure 40: Representative image of cracking observed in resin in Panel 2

The cross-section images of panel 3 are shown in Figures 41-44. The images from panel 3 show areas of voids in between many of the plies. Panel 3 also shows similar characteristics observed in the other panels. The ultrasonic indications in panel 3 correlate to several areas of porosity, although it is not clear if one specific area resulted in the indication.

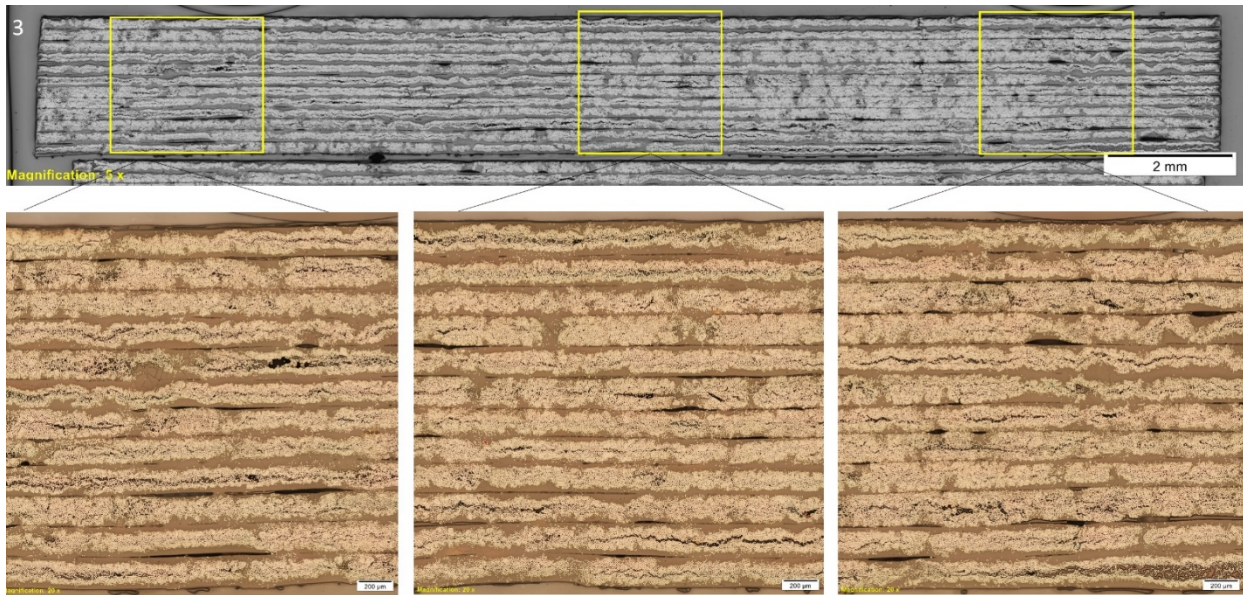


Figure 41: Panel 3, Section 1 low magnification view and high magnification view of left, center, and right areas

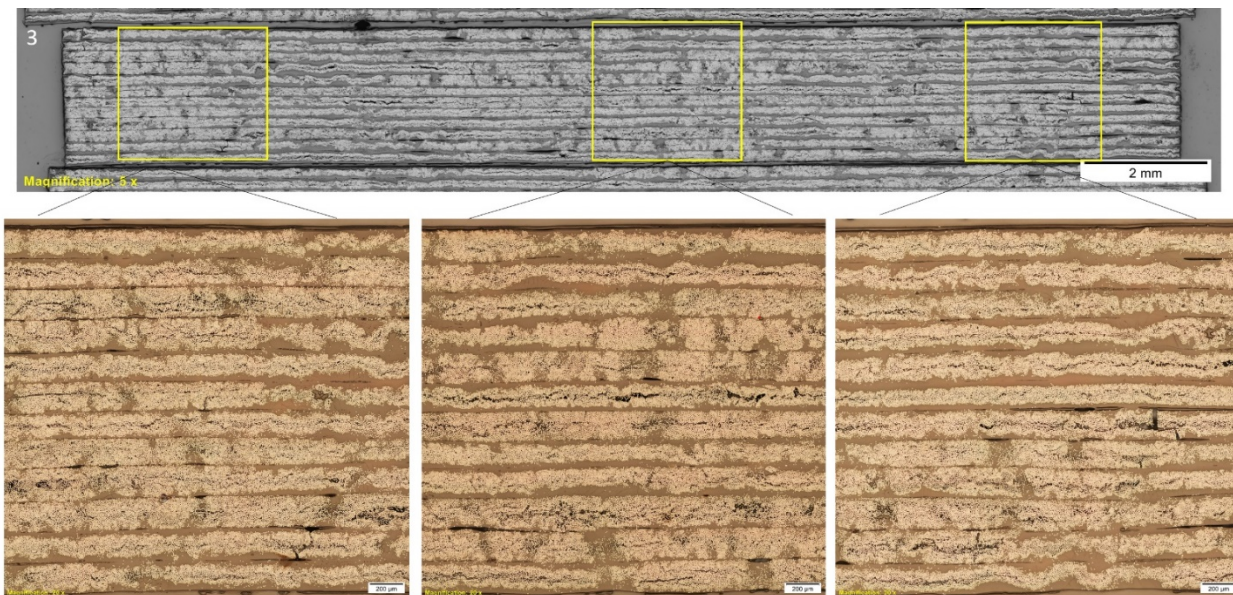


Figure 42: Panel 3, Section 2 low magnification view and high magnification view of left, center, and right areas

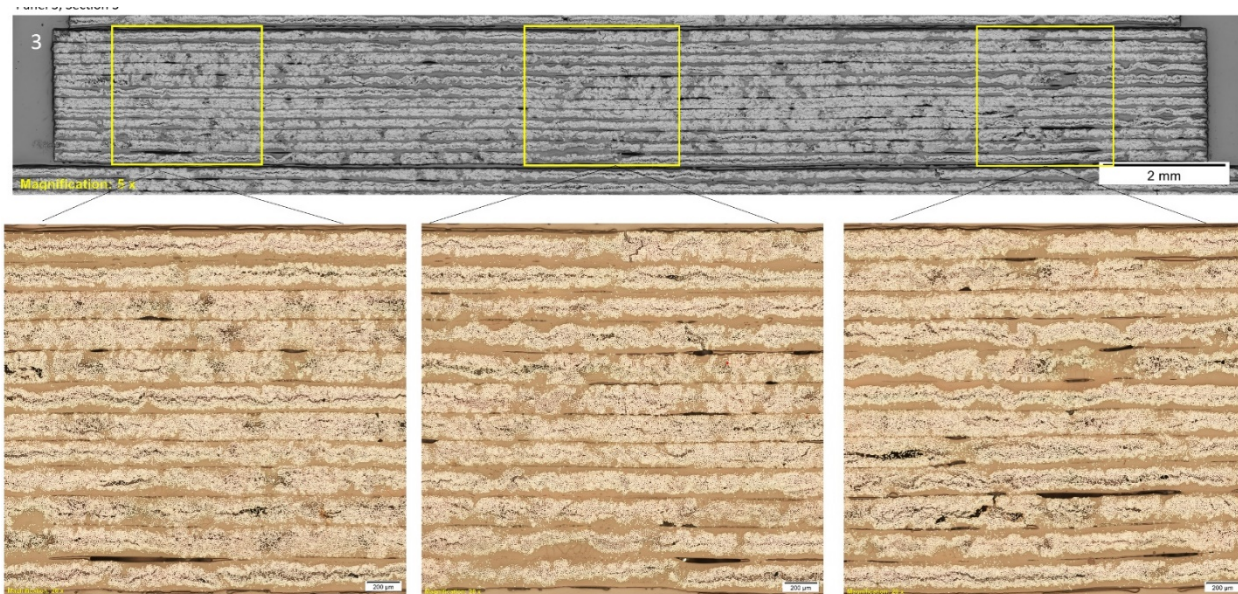


Figure 43: Panel 3, Section 3 low magnification view and high magnification view of left, center, and right areas

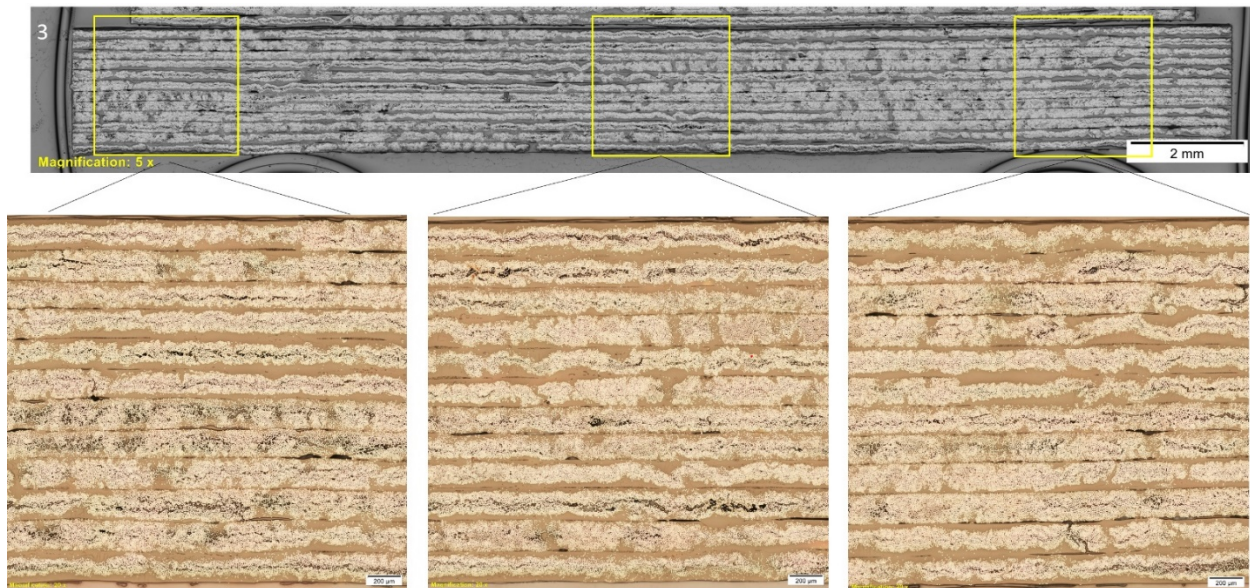


Figure 44: Panel 3, Section 4 low magnification view and high magnification view of left, center, and right areas

Conclusions of cross-sectional analysis

The following conclusions are based on the cross-section analysis:

- All panels demonstrated regions of porosity, resin richness, inconsistent fiber bundle spread and fiber waviness
- Resin cracking was observed in all panels but was most prevalent in panel 2

- The voids present in between the plies of panel 3 indicate that complete consolidation was not achieved

References

1. Hughes, M.S., *Analysis of Ultrasonic Waveforms Using Shannon Entropy*. 1992 IEEE Ultrasonics Symposium, 1992. **92CH3118-7**: p. 1205-1209.
2. Hughes, M.S., et al., *Application of Renyi entropy for ultrasonic molecular imaging*. J Acoust Soc Am, 2009. **125**(5): p. 3141-5.
3. Hughes, M.S., et al., *Properties of an entropy-based signal receiver with an application to ultrasonic molecular imaging*. J Acoust Soc Am, 2007. **121**(6): p. 3542-57.
4. Hughes, M.S., et al., *Real-time Calculation of a Limiting form of the Renyi Entropy Applied to Detection of Subtle Changes in Scattering Architecture*. J Acoust Soc Am, 2009. **126**(5): p. 2350-2358.
5. Wallace, K.D., et al., *Sensitive Ultrasonic Delineation of Steroid Treatment in Living Dystrophic Mice with Energy-Based and Entropy-Based Radio Frequency Signal Processing*. IEEE Transactions on Ultrasonics, Ferroelectrics and Frequency Control, 2007. **54**(11): p. 2291-2299.
6. Larche, M., et al., *High Sensitivity Imaging of Resin-Rich Regions in Graphite/Epoxy Laminates using Joint-Entropy*. Proceedings Volume 10169, Nondestructive Characterization and Monitoring of Advanced Materials, Aerospace, and Civil Infrastructure.
7. Cover, T.M. and J.A. Thomas, *Elements of Information Theory*. 1991, New York: wiley-Interscience.
8. Hughes, M.S., et al., *Characterization of Digital Waveforms Using Thermodynamic Analogs: Applications to Detection of Materials Defects*. I.E.E.E Transactions on Ultrasonics, Ferroelectrics, and Frequency Control, 2005.
9. Schwartz, L., *Mathematics for the Physical Sciences*. 2008, Mineola, New York: Dover. pp 368.
10. Hughes, M.S., et al., *Joint-Entropy of Continuously Differentiable Ultrasonic Waveforms*. Journal of the Acoustical Society of America, 2013. **33**(1): p. 283-300.
11. Hughes, M., et al., *Entropy vs. Energy Waveform Processing: A Comparison Based on the Heat Equation*. Entropy, 2015. **17**(6): p. 32.
12. Hughes, M.S., *A Comparison of Shannon Entropy versus Signal Energy for Acoustic Detection of Artificially Induced Defects in Plexiglass*. Journal of the Acoustical Society of America, 1992. **91**(4): p. 2272-2275.
13. Hughes, M.S., *Analysis of Digitized Waveforms Using Shannon Entropy*. Journal of the Acoustical Society of America, 1993. **93**(4): p. 892-906.

Pacific Northwest National Laboratory

902 Battelle Boulevard
P.O. Box 999
Richland, WA 99354
1-888-375-PNNL (7665)

www.pnnl.gov